

APPEARANCE BASED RENDERING

by

HAROLD BRUCE WESTLUND

A THESIS

Presented to the Department of Computer  
and Information Science  
and the Graduate School of the University of Oregon  
in partial fulfillment of the requirements  
for the degree of  
Master of Science

December 2000

“Appearance Based Rendering,” a thesis prepared by Harold Bruce Westlund in partial fulfillment of the requirements for the Master of Science degree in the Department of Computer and Information Science. This thesis has been approved and accepted by:

---

Dr. Gary W. Meyer

---

Date

Accepted by:

---

Dean of the Graduate School

An Abstract of the Thesis of  
Harold Bruce Westlund for the degree of Master of Science  
in the Department of Computer and Information Science  
to be taken December 2000  
Title: APPEARANCE BASED RENDERING

Approved: \_\_\_\_\_  
Dr. Gary W. Meyer

Industry standard methods for measuring appearance are applied to realistic image synthesis. Two appearance attributes, gloss and haze, are known to be determined by the shape of the specular reflection lobe. Standards which specify the measurement of these two geometric appearance attributes are used to select BRDF model parameters for a number of computer graphics reflection models. The bi-directional reflectance distribution function (BRDF) of metallic and pearlescent paints can be characterized with only a few industry standard specular measurements. Using these measurements, a new computer graphics BRDF model is developed.

The Beard-Maxwell BRDF model, which utilizes a systematic measurement protocol to determine appropriate model parameter values, is presented. An associated database containing parameters for hundreds of measured surfaces, is overviewed. Also, a new method of Monte Carlo importance sampling is described which allows importance sampling of arbitrary BRDFs.

## CURRICULUM VITA

NAME OF AUTHOR: Harold Bruce Westlund

PLACE OF BIRTH: Champaign, Illinois

DATE OF BIRTH: April 7, 1967

### GRADUATE AND UNDERGRADUATE SCHOOLS ATTENDED:

University of Oregon

### DEGREES AWARDED:

Master of Science in Computer and Information Science, 2000

Bachelor of Science in Computer Science, 1998

Bachelor of Science in Mathematics, 1997

### AREAS OF SPECIAL INTEREST:

Realistic Image Synthesis

### PROFESSIONAL EXPERIENCE:

Research Assistant, Department of Computer and Information Science,  
University of Oregon, Eugene, 1999–2000

Teaching Assistant, Department of Computer and Information Science,  
University of Oregon, Eugene, 1998

## ACKNOWLEDGEMENTS

Thank you to my advisor, Professor Gary Meyer. His motivation, patience, and keen insight proved critical to the successful completion of this thesis.

Thank you to fellow students Aaron Pfeiffer, Peter Walker, and Joseph Wingard for their many helpful discussions.

Thank you to Mom and Dad, who have always been there to support me.

## DEDICATION

To my wife Tanya. Without your sacrifice and encouragement, the following pages would be blank.

## TABLE OF CONTENTS

Chapter	Page
I. INTRODUCTION . . . . .	1
II. MONTE CARLO BRDF SHADER . . . . .	5
BRDF . . . . .	5
Radiance . . . . .	7
Monte Carlo Importance Sampling . . . . .	9
Alias Method . . . . .	13
iBRDF . . . . .	18
III. RENDERING WITH NEFDS . . . . .	21
NEF Reflection Model . . . . .	22
NEFDS . . . . .	32
Rendering Data . . . . .	41
IV. APPEARANCE BASED MEASUREMENTS . . . . .	47
Subsurface Highlights - Flop . . . . .	47
First Surface Reflection - Gloss and Haze . . . . .	56
Combining First Surface and Flop . . . . .	76
V. CONCLUSION . . . . .	80
BIBLIOGRAPHY . . . . .	83

## LIST OF FIGURES

Figure	Page
1. Light Reflection Geometry . . . . .	6
2. Alias Method Setup Procedure . . . . .	17
3. First Surface Reflection Off Micro-Facets . . . . .	24
4. Half Angle Geometry . . . . .	25
5. Main Menu of <i>NefMenu</i> . . . . .	34
6. Material Selection Menu of <i>NefMenu</i> . . . . .	35
7. BRDF Parameters Menu of <i>NefMenu</i> , Page 1 . . . . .	36
8. BRDF Parameters Menu of <i>NefMenu</i> , Page 2 . . . . .	37
9. Spectral Reflectance Function for Material 0880, Yellow Paint . . . . .	38
10. Spectral Reflectance Function for Material 0221, Red Dirt . . . . .	39
11. Raw Spectral Reflectance Values for Material 0880, Yellow Paint . . . . .	40
12. Spectral and Spatial Parameters Used to Generate Figure 13 for Material 0880, Yellow Paint . . . . .	41
13. Spectral BRDF Values for Material 0880, Yellow Paint . . . . .	42
14. Command Line Request to <i>BRDF</i> . . . . .	43
15. Vases with NEF Materials Bare Construction Lumber, Gloss Paint on Metal, and Scored Aluminum . . . . .	45
16. Vases with Textured NEF Materials Bare Construction Lumber, Gloss Paint on Metal, and Scored Aluminum . . . . .	45
17. Cubes with Textured NEF materials Cement, Gloss Paint on Metal, Bare Construction Lumber, Scored Aluminum, and Weathered Concrete . . . . .	46
18. Subsurface Structure of Metallic Paint . . . . .	48
19. Subsurface Structure of Pearlescent Paint . . . . .	49



	Page
20. Observed Radiance Using Full Spectral Method . . . . .	52
21. Observed Radiance Using Simplified Spectral Method . . . . .	52
22. Observed Tristimulus Values Using Normal RGB Method . . . . .	54
23. Observed Tristimulus Values Using Simplified RGB Method . . . . .	54
24. $L^*$ Values Vs. Aspecular Angle for Metallic Paint Samples . . . . .	56
25. $a^*$ Values Vs. Aspecular Angle for Metallic Paint Samples . . . . .	57
26. $b^*$ Values Vs. Aspecular Angle for Metallic Paint Samples . . . . .	57
27. $\rho_R(\theta_\alpha)$ Vs. $\theta_\alpha$ of Metallic Paint Samples . . . . .	58
28. $\rho_G(\theta_\alpha)$ Vs. $\theta_\alpha$ of Metallic Paint Samples . . . . .	58
29. $\rho_B(\theta_\alpha)$ Vs. $\theta_\alpha$ of Metallic Paint Samples . . . . .	59
30. Three Vases with Metallic Paint . . . . .	59
31. Three More Vases with Metallic Paint . . . . .	60
32. Numerical Gloss Values Vs. Visual Gloss Rating for ASTM Specular Gloss Standards . . . . .	62
33. Subdivision of Source and Recepture Apertures Using 60 Degree Gloss Specifications . . . . .	65
34. Flux Passing Through Receptor Apterture Due to One Source Aperture Subdision . . . . .	65
35. 20 Degree Specular Gloss Values Vs. Roughness from the Ward Model . .	67
36. Gloss Vs. Roughness for Ward Isotropic Reflection Model . . . . .	72
37. Haze Vs. Roughness for Ward Isotropic Reflection Model . . . . .	74
38. Tiles with Measured 20 Degree Specular Gloss Values 20, 40, 60, and 80 .	75
39. Tiles With Measured 20 Degree Specular Gloss Values 10, 30, 50, 70, and 90 . . . . .	75
40. Photograph of Clear Coat Finish on Metallic Paint . . . . .	76

	Page
41. Three Vases with Metallic Paint and a First Surface of Gloss 100 . . . . .	77
42. Three More Vases with Metallic Paint and a First Surface of Gloss 100 . .	78
43. Two Red Automotive Shells with 20 Degree Specular Gloss of 10 and 60	78
44. Two Dark Blue Automotive Shells with 20 Degree Specular Gloss of 10 and 60 . . . . .	79
45. Two Medium Blue Automotive Shells with 20 Degree Specular Gloss of 10 and 60 . . . . .	79

## LIST OF TABLES

Table	Page
1. Standard Gloss and Haze Measurement Specifications . . . . .	63
2. 20 Degree Specular Gloss Values Computed from the Ward Model Over a Range of Roughness Values . . . . .	66
3. Gloss and Haze Values Computed from the Ward Model Over a Range of Roughness Values . . . . .	73
4. Interpolated 20 Degree Specular Gloss Values for Ward Isotropic Reflection Model . . . . .	74

## CHAPTER I

### INTRODUCTION

Realistic image synthesis involves the simulation of a real world environment and the determination of what a human observer in that environment would see. The key elements of the simulation are the sources of light, the geometry and position of objects, and the light scattering properties of those objects. The degree to which the simulation accurately mimics the physics governing the real world and the psycho-physical attributes of the human observer determines the accuracy of the realistic image synthesis process [28].

The question of what light reaches the observer can be answered solely on the basis of physics. Kajiya [35] articulated this problem with the rendering equation, specifying the relationship between the energy leaving a surface and the incoming energy from the rest of the environment. When applied to every surface the resulting collection of equations completely determines the behavior of light in the global environment. Once this global illumination problem is solved, the light reaching the observer can be calculated and an image generated. The two main methods which have been utilized to approximate the solution to this global illumination problem are ray tracing [77] and radiosity [27]. In this thesis an advanced physically-based ray tracer is utilized [74]. However, both ray tracing and radiosity are approximations to the same global illumination problem, so most of the work discussed in this thesis is applicable to both image synthesis methods.

The rendering equation specifies that the radiance leaving a surface is the integrated value of light impinging upon the surface modified by the surface's bi-directional reflection distribution function (BRDF). This integral can be quite difficult to solve both because the incoming radiance is not fully known and also because the surface's BRDF is very complex. Monte Carlo integration is often called upon to solve this integral but this can result in high variance. Variance reduction has been performed with the use of importance sampling [40, 43]. However, this technique has previously required the BRDF to take the form of an inevitable function, thus limiting the technique's applicability. The first contribution of this thesis is the generalization of Monte Carlo importance sampling to arbitrary BRDFs. This new Monte Carlo method, which utilizes properties of discretely sampled BRDFs, is detailed, and a specific implementation of this technique is presented.

Accurate realistic image synthesis is dependent upon the accuracy of the local illumination model. Even if the rendering equation is solved exactly, inaccurate BRDFs will lead to an incorrect image. However, selecting a BRDF model and choosing the appropriate parameter values which faithfully represent the reflection properties of a real world surface is a difficult task. A simple BRDF model will allow for easy parameter selection but often will result in an inaccurate representation. On the other hand, a complex model offers the ability to represent a wide variety of surfaces but the correct selection of parameter values can be daunting. The fitting of model parameters to measured data is also quite difficult, often achieved only through trial and error rather than through systematic techniques.

The second contribution of this thesis is discussion of Maxwell and Beard's empirical BRDF model [45] and a BRDF database built on an extension to their model [48].

The BRDF model utilized by the database contains many of the physically based attributes used in more advanced BRDF models, including Fresnel effects and directional diffuse scattering. It is empirically motivated; the model parameters are selected through the use of a well defined measurement protocol. By selecting only relevant measurements, the model achieves higher accuracy with fewer measurements than is possible with purely analytical models. Additionally, the BRDF database contains the parameters corresponding to hundred of surfaces which can be of immediate benefit to the computer graphics community.

Even with the increased measurement efficiency offered by the empirical Beard-Maxwell BRDF model, the number of measurements required to select BRDF model parameters may still be too high. One way to significantly reduce the number of required measurements is to put constraints on the types of surfaces which the model may represent. This technique was used to create a new representation of light reflection for metallic and pearlescent paints. It incorporates industry standards which allow characterization of these surfaces using only a few key measurements. With this model, the spectral variation of the specular reflection is fully characterized. This new reflection model, tailored for metallics and pearlescents through the use of standard measurements, is the next contribution.

Many of the intuitive appearance characteristics that we assign to surfaces, such as glossiness and haziness, have well defined standard measurements. These widely used appearance standards give numerical values to the geometric attributes of the surface reflection of light. While the metallic and pearlescent measurement techniques account for the spectral distribution of specular reflection, these standards quantify the magnitude and shape of specular reflection. In addition, the gloss and haze standards are all

well established and practiced, some having been set over 60 years ago. The appearance information obtained from the gloss and haze measurements can be used to guide the selection of appropriate BRDF model parameters. The final contribution of this thesis is a discussion of these appearance standards and methods for utilizing them in parameter selection.

The remainder of this thesis is divided into four additional chapters. Chapter II presents a new Monte Carlo importance sampling technique for use with discretely sampled BRDFs. In chapter III an empirical BRDF model is reviewed as is a database system containing parameters for hundreds of surfaces. Chapter IV offers a discussion of standard appearance measurements currently used in industry and their applicability to realistic image synthesis. Lastly, a summary and concluding remarks is given in chapter V.

## CHAPTER II

### MONTE CARLO BRDF SHADER

Given a description of the reflective properties of a surface, we want to be able to render a synthetic image of that surface. Since we are interested in comparing real world surfaces with synthetically generated surfaces, the reflective properties should be describable either discretely or analytically. It would be advantageous to have the ability to create images using any description of surface reflection. In this chapter we explain how an arbitrary reflection model can be used to generate synthetic images.

#### BRDF

One of the most general forms of the reflection model is the bi-directional reflection distribution function (BRDF), a function which defines the spectral and spatial reflection characteristic of a surface. Loosely speaking, the BRDF is the ratio of directionally reflected light to directionally incident light at a particular wavelength. More precisely, the BRDF is defined as:

$$\rho(\Theta_i; \Theta_r; \lambda) = \frac{dL_r(\Theta_i; \Theta_r; \lambda)}{dE_i(\Theta_i; \lambda)} \quad (2.1)$$

where the subscripts i and r denote incident and reflected respectively,  $\Theta$  is the direction of light propagation,  $\lambda$  is the wavelength of light, L is radiance, and E is irradiance [50]. The geometry used by the BRDF is shown in Figure 1.



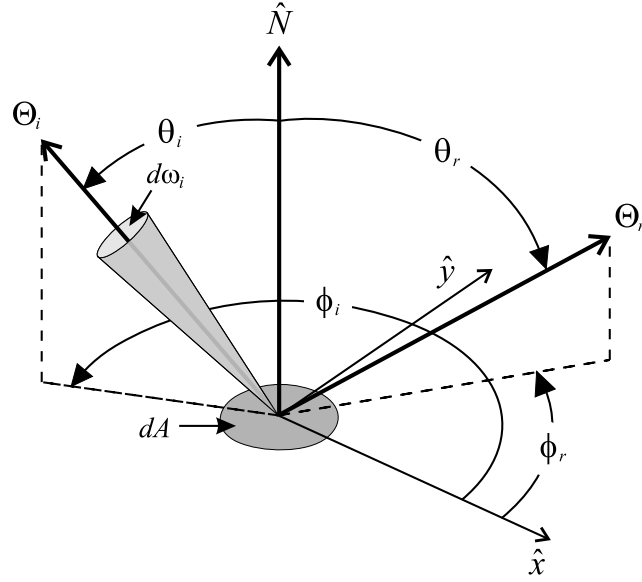


FIGURE 1. Light reflection geometry

Irradiance is related to radiance by

$$\begin{aligned} dE(\Theta) &= L(\Theta)(\Theta \cdot \hat{n})d\omega \\ &= L(\Theta)d\Omega \end{aligned} \quad (2.2)$$

where  $\hat{n}$  is the surface normal and  $d\omega$  is the solid angle in which the radiance is confined. For notational convenience the projected solid angle,  $d\Omega$ , will be used rather than the solid angle. Reworking (2.1) we can use the BRDF to evaluate the radiance reflected off a surface by

$$\begin{aligned} dL_r(\Theta_i; \Theta_r; \lambda) &= \rho(\Theta_i; \Theta_r; \lambda)dE_i(\Theta_i; \lambda) \\ &= \rho(\Theta_i; \Theta_r; \lambda)L_i(\Theta_i; \lambda)d\Omega_i \end{aligned} \quad (2.3)$$

The total radiance reflected in direction  $\Theta_r$  can then be found by integrating (2.3) over

all incident directions.

$$L_r(\Theta_r; \lambda) = \int_{\Omega_i} \rho(\Theta_i; \Theta_r; \lambda) L_i(\Theta_i; \lambda) d\Omega_i \quad (2.4)$$

By adding the radiance due to self emission to (2.4) we obtain Kajiya's rendering equation [35]

$$L_r(\Theta_r; \lambda) = L_e(\Theta_r) + \int_{\Omega_i} \rho(\Theta_i; \Theta_r; \lambda) L_i(\Theta_i; \lambda) d\Omega_i. \quad (2.5)$$

Kajiya presented (2.5) using the energy transfer between points rather than using radiance, otherwise they are the same. Kajiya showed that generating an approximation of the global solution to this equation is the basis of most photorealistic rendering algorithms.

The reference wavelength will be dropped from the parameter list of all equations for the remainder of this chapter unless specifically referenced. However, it should be understood that the wavelength is implicitly included. For the following discussion, results from two different wavelengths of light must be treated as completely uncorrelated.

### Radiance

The Radiance Lighting Simulation and Rendering System (Radiance) [42, 74] was used to generate the synthetic images in this thesis. Radiance is a suite of programs built around an advanced distributed raytracer designed for realistic image synthesis. It was selected because it is a physically-based rendering system designed to accurately model the light behavior of a scene using physical units [74]. This is advantageous for comparing real world scenes to their virtual counterparts. Also, the source code is

publicly available [54] and the program is currently in wide use, aiding future work.

In Radiance, the integrated region  $\Omega_i$  of (2.4) is partitioned into the area subtended by the light sources,  $\Omega'_i$ , and the remaining area,  $\Omega''_i$ . (2.4) can then be written as

$$L_r(\Theta_r) = \int_{\Omega'_i} \rho(\Theta_i; \Theta_r) L_i(\Theta_i) d\Omega'_i + \int_{\Omega''_i} \rho(\Theta_i; \Theta_r) L_i(\Theta_i) d\Omega''_i \quad (2.6)$$

The location, size and intensity of all the light sources are used to find the potential contribution of each source to the first integral of (2.6). In Radiance the total radiance due to the light sources is cleverly approximated using the direct contribution of the greatest potential contributors and cached prior values [73]. Because this integral often comprises the largest portion of the total reflected radiance, solving it separately increases overall program efficiency.

Radiance also separates the BRDF of the second integral into two components, diffuse and specular. The diffuse component refers only to pure Lambertian while specular refers to the remainder of the BRDF. Lambertian reflectance is the ideal approximation of a matte surface, having a constant value independent of incident and reflected angles for each wavelength [41]. The BRDF written as the sum of diffuse and specular components then becomes

$$\rho(\Theta_i; \Theta_r) = \rho_d + \rho_s(\Theta_i; \Theta_r).$$

Thus (2.6) can be rewritten

$$\begin{aligned}
L_r(\Theta_r) &= \int_{\Omega'_i} \rho(\Theta_i; \Theta_r) L_i(\Theta_i) d\Omega'_i + \\
&\quad \int_{\Omega''_i} [\rho_d + \rho_s(\Theta_i; \Theta_r)] L_i(\Theta_i) d\Omega''_i \\
&= \int_{\Omega'_i} \rho(\Theta_i; \Theta_r) L_i(\Theta_i) d\Omega'_i + \\
&\quad \int_{\Omega''_i} \rho_d L_i(\Theta_i) d\Omega''_i + \int_{\Omega''_i} \rho_s(\Theta_i; \Theta_r) L_i(\Theta_i) d\Omega''_i \quad (2.7)
\end{aligned}$$

The advantage of this separation is that the diffusely reflected radiance (i.e., the second integral of (2.7)) is slowly varying across the surface. Radiance utilizes this by caching the diffusely reflected radiance values and interpolating between those cached results whenever possible [76, 75]. Additionally, since the diffuse reflectance is pure Lambertian, the cached values are valid for all reflected angles.

The last integral of (2.7) is the radiance produced by indirect specular reflection from non-light sources in the environment. Variations in the irradiance values and the BRDF make direct integration of this integral inefficient. To evaluate this integral, Radiance uses Monte Carlo importance sampling.

### Monte Carlo Importance Sampling

Monte Carlo integration is a method of numerical integration which uses random variates to produce an estimate of an integral. Monte Carlo integration is particularly appropriate for both irregular and multidimensional integrals.

The type of Monte Carlo integration that will be discussed here is Monte Carlo importance sampling, which as the name implies, samples the integrand densely at “more important” points. The “more important” points are those where the integrand has large

values. The key insight of Monte Carlo importance sampling is that an expected value can be used to represent an integral. Thus the integral can be estimated by finding the expected value.

Consider the function  $g : \mathbb{R}^n \rightarrow \mathbb{R}$ , integrated over the region  $\Omega \subset \mathbb{R}^n$ ,

$$I = \int_{x \in \Omega} g(x) d\Omega(x). \quad (2.8)$$

By carefully selecting an appropriate probability density function (p.d.f.), (2.8) can be rewritten as

$$I = \int_{x \in \Omega} \frac{g(x)}{f_X(x)} f_X(x) d\Omega(x) \quad (2.9)$$

where  $f_X(x)$  is the p.d.f. chosen so that  $f_X(x) > 0$  whenever  $g(x) \neq 0$ . If the random variate  $\mathbf{X}$  is distributed with  $f_X(x)$  (this relationship denoted by  $\mathbf{X} \sim f$ ) then the integral can be represented by the expected value

$$I = E \left[ \frac{g(\mathbf{X})}{f_X(\mathbf{X})} \right]. \quad (2.10)$$

An approximation to the expected value of (2.10) (and thus the integral) can be found by calculating the sample mean derived from a sequence of  $N$  random variates  $\mathbf{X}_i \sim f$ ,

$$I = E \left[ \frac{g(\mathbf{X})}{f_X(\mathbf{X})} \right] \approx \frac{1}{N} \sum_{i=1}^N \frac{g(\mathbf{X}_i)}{f_X(\mathbf{X}_i)} \quad (2.11)$$

In fact, by the Law of Large Numbers [23], the approximation becomes an equality as  $N$  approaches infinity:

$$I = E \left[ \frac{g(\mathbf{X})}{f_X(\mathbf{X})} \right] = \lim_{N \rightarrow \infty} \frac{1}{N} \sum_{i=1}^N \frac{g(\mathbf{X}_i)}{f_X(\mathbf{X}_i)} \quad (2.12)$$

The approximation obtained in (2.11) has an error which is measurable by the variance of the sample mean:

$$\begin{aligned}
 \text{var} \left( \frac{1}{N} \sum_{i=1}^N \frac{g(X_i)}{f_X(X_i)} \right) &= \frac{1}{N^2} \sum_{i=1}^N \text{var} \left( \frac{g(X_i)}{f_X(X_i)} \right) \\
 &= \frac{1}{N^2} \sum_{i=1}^N \text{var} \left( \frac{g(X)}{f_X(X)} \right) \\
 &= \frac{1}{N} \text{var} \left( \frac{g(X)}{f_X(X)} \right). \tag{2.13}
 \end{aligned}$$

This makes obvious why the p.d.f.  $f_X(x)$  should be chosen carefully. The closer  $f$  matches  $g$ , the lower the variance. In fact, if  $f_X(x) \propto g(x)$  over  $\Omega$ , there is zero variance produced by the sampling process. (Of course if  $g$  is known this precisely, there is no point in using Monte Carlo integration.)

To approximate the last integral of (2.7) using Monte Carlo importance sampling, select the p.d.f. to be the BRDF normalized over  $\Omega_i''$ <sup>1</sup>:

$$\begin{aligned}
 f_{\Theta_i}(\Theta_i; \Theta_r) &= \frac{\rho_s(\Theta_i; \Theta_r)}{\int_{\Omega_i''} \rho_s(\Theta_i; \Theta_r) d\Omega_i''} \\
 &= \frac{\rho_s(\Theta_i; \Theta_r)}{R_{\Omega_i''}(\Theta_r)} \tag{2.14}
 \end{aligned}$$

---

<sup>1</sup>Radiance implements this by normalizing the BRDF over the entire hemisphere and rejecting any point selected in  $\Omega_i'$ . This does not become too inefficient since the total area subtended by the light sources in a scene is typically a small fraction of the hemisphere (i.e.,  $\Omega_i \approx \Omega_i'$ ).

Now select a sequence of random variates  $\Theta_i \sim f_{\Theta_i}$  and apply (2.11):

$$\begin{aligned}
\int_{\Omega_i''} \rho_s(\Theta_i; \Theta_r) L_i(\Theta_i) d\Omega_i'' &\approx \frac{1}{N} \sum_{i=1}^N \frac{\rho_s(\Theta_i; \Theta_r) L_i(\Theta_i)}{f_{\Theta_i}(\Theta_i; \Theta_r)} \\
&= \frac{1}{N} \sum_{i=1}^N \frac{\rho_s(\Theta_i; \Theta_r) L_i(\Theta_i)}{\rho_s(\Theta_i; \Theta_r) / R_{\Omega_i''}(\Theta_r)} \\
&= \frac{R_{\Omega_i''}(\Theta_r)}{N} \sum_{i=1}^N L_i(\Theta_i) \tag{2.15}
\end{aligned}$$

The variance in the approximation of (2.15) is

$$\text{var} \left( \frac{R_{\Omega_i''}(\Theta_r)}{N} \sum_{i=1}^N L_i(\Theta_i) \right) = \frac{R_{\Omega_i''}^2(\Theta_r)}{N} \text{var} (L_i(\Theta)). \tag{2.16}$$

The variance of the approximation is thus driven by the variance of the incident radiance. The hope is that the separation of  $\Omega_i$  in (2.6) will result in incident radiance of only low variance across  $\Omega_i''$ .

In Radiance, the BRDF was chosen in large part to provide an easy, analytical method for obtaining the random variates required by (2.14) to perform Monte Carlo importance sampling. In general the inverse  $F^{-1}(x)$  of a cumulative distribution function (c.d.f.)

$$F(x) = Pr(\mathbf{X} \leq x), \mathbf{X} \sim f$$

can be used to produce  $\mathbf{X} \sim f$  from uniformly distributed variate  $\mathbf{u} \sim U(0, 1)$  by

$$\mathbf{X} = F^{-1}(\mathbf{u}).$$

Radiance utilizes this inverse method by using a BRDF built around the normal p.d.f., which has an easily invertible c.d.f. (for instance see Rubinstein [60]).

The isotropic version of the BRDF in Radiance is

$$\rho_{iso}(\Theta_i; \Theta_r) = \frac{\rho_d}{\pi} + \rho_s \frac{1}{\sqrt{\Theta_i \cdot \hat{n}} \Theta_r \cdot \hat{n}} \frac{\exp[-\tan^2(\delta/\alpha^2)]}{4\pi\alpha^2} \quad (2.17)$$

where  $\rho_d$  is the diffuse reflectance,  $\rho_s$  is the specular reflectance,  $\delta$  is the angle between surface normal,  $\hat{n}$ , and the half vector between the incident and reflected directions,  $\hat{h}$ , and  $\alpha$  is the standard deviation (RMS) of the surface slope [43]. The inversion method is used to create the required random variate  $\Theta = (\delta, \phi) \sim f_{iso}$  from  $\mathbf{u}_1 \sim U(0, 1)$  and  $\mathbf{u}_2 \sim U(0, 1)$  by

$$\delta = \alpha[-\log(\mathbf{u}_1)]^{1/2}$$

$$\phi = 2\pi\mathbf{u}_2$$

where  $\phi$  is the random variate corresponding to the azimuthal angle. A similar albeit more complicated version of the BRDF and the inversion process is also used in Radiance for anisotropic reflection [73].

### Alias Method

The inverse method is used to generate random variates of the p.d.f corresponding to the BRDF in Radiance. In general, analytically generating random variates of arbitrary p.d.f.s is not possible. However, there are techniques available to create the random variates of arbitrary probability mass functions (p.m.f.s), the discretized counterpart to the p.d.f. Gentle [26] and Knuth [36] both offer a nice overview and discussion of the many methods available. For this thesis, the alias method proposed by Walker [70, 69, 71] was selected because it generates random variates in constant time.



Many variations of Walker's original model have been proposed offering advantages in one way or another [24, 38, 37, 39, 52, 68]. The modification by Vose [68] was chosen because it allows for initialization in  $O(N)$  time versus the original paper's time of  $O(N \log N)$ . Vose also presents several optimizations for memory and execution time although they are not used here.

The alias method is most easily viewed as a form of the rejection method in which the rejected values are recycled into usable data. It requires an initial setup which need only be performed once. After the setup is complete random variates are created by transforming variates of a uniform distribution. The following discussion offers an explanation of both the setup and creation steps, and some examples are provided.

Consider the random variate  $\mathbf{X}$  which can take on any of the  $k$  values,

$$X = \{x_1, x_2, \dots, x_k\} \quad (2.18)$$

with corresponding probability

$$P = \{p_1, p_2, \dots, p_k\}. \quad (2.19)$$

Ensure that the probabilities form a valid p.m.f. by requiring that  $\sum_{i=1}^k p_i = 1$ .

In the setup process, the alias method creates two new lists, the rejection list and the alias list. The rejection list is a list of probabilities,

$$R = \{r_1, r_2, \dots, r_k\}, \quad (2.20)$$

whose elements  $r_i$  determine whether or not an alias is to be used. Each probability  $r_i$

in the rejection list forms its own p.m.f. together with its complement,  $1 - r_i$ . The alias list,

$$A = \{a_1, a_2, \dots, a_k\}, \quad (2.21)$$

consists of  $k$  indices which each may take on integer values 1 through  $k$ , representing the index of the alias. The setup process, described in more detail below, is performed only once.

After the setup has been completed, selection of the random variate  $\mathbf{X}$  is performed by choosing two uniformly distributed variates,  $\mathbf{u} \sim U(0, 1)$  and  $\mathbf{i} \sim U_d(1, k)$ , where  $U_d(1, k)$  is a discrete uniform distribution over the integers 1 through  $k$ .  $\mathbf{X}$  is given the value  $x_i$  if  $\mathbf{u} \leq r_i$  ( $\mathbf{u}$  was not rejected).  $\mathbf{X}$  is given the value  $x_{a_i}$  if  $\mathbf{u} > r_i$  ( $\mathbf{u}$  was rejected so the alias was used). The time required to generate this random variate is equal to the total time required to generate  $\mathbf{u}$ , perform a comparison, and then lookup the final value. Assuming these three actions can be performed in constant time, so can the generating step.

A few examples are now given here to further clarify the above discussion.

Let  $X = \{.125, .025, .15, .05, .15\}$  and  $P = \{.25, .05, .3, .1, .3\}$ . The setup method discussed in detail below creates the rejection list  $R = \{1, .25, .75, .5, 1\}$  and the alias list  $A = \{1, 3, 1, 5, 5\}$ .

Suppose the random variates are selected to be  $\mathbf{i} = 3$  and  $\mathbf{u} = .74$ . Then since  $\mathbf{u} \leq r_3 = .75$ ,  $\mathbf{X}$  is assigned the value  $x_3 = .15$ . However if the random variates are selected to be  $\mathbf{i} = 3$  and  $\mathbf{u} = .76$ ,  $\mathbf{u} > r_3$  and so  $\mathbf{X}$  is assigned the value  $x_{a_3=1} = .15$ . In the later case  $\mathbf{u}$  is rejected so the alias is used.

Now suppose instead that the random variates are selected to be  $\mathbf{i} = 5$  and  $\mathbf{u} = .23$ . Since  $\mathbf{u} \leq r_1 = 1$ ,  $\mathbf{X}$  is assigned the value  $x_5 = .15$ . In fact  $\mathbf{X}$  will always be assigned

the value  $x_i$  when  $r_i = 1$ . Likewise  $\mathbf{X}$  will always be assigned the value  $x_{a_i}$  when  $r_i = 0$ .

The setup will now be described in full detail. The goal of the setup is to even out the probabilities of list  $P$  so that each item has combined probability of exactly  $\frac{1}{k}$  between itself and its alias.

Partition the  $k$  indices of the lists  $X$  and  $P$  into two sets, large and small by

$$small = \{i : p_i < \frac{1}{k}\} \quad (2.22)$$

$$large = \{i : p_i \geq \frac{1}{k}\}. \quad (2.23)$$

An item in the small set will need to have its alias pointing to an item in the large set in order to achieve the desired combined probability of  $\frac{1}{k}$ . Select one item from each of the two lists.

The selection process begins by giving (via the alias) the small element enough probability mass from the large element so that it has a combined probability of  $\frac{1}{k}$ . After aliasing the probability mass, the smaller item will have a combined probability of  $\frac{1}{k}$ , so it is finished. The newly adjusted large element will then either belong to the large or the small set (note that a probability of exactly  $\frac{1}{k}$  will place it in the large set). Repeat the selection process using the adjusted large item and an item belonging to the other set until all the lists  $A$  and  $R$  are complete.

The setup phase is shown in Figure 2 as pseudo-code as described in [68]. The last two lines are to correct any rounding errors which may crop up when using finite precision floats. As is clear from this pseudo-code, the total time for setup is proportional to the list size, (i.e.,  $O(N)$ ).

Consider a BRDF discretely sampled at  $j$  reflected directions  $\{\Theta_{r,1}, \Theta_{r,2}, \dots, \Theta_{r,j}\}$ ,

```

l = 0; s = 0
for i = 0 to k - 1
if pi > 1/k
then largel = i; l = l + 1
else smalls = i; s = s + 1
while s ≠ 0 and l ≠ 0
s = s - 1; i = smalls
l = l - 1; j = largel
probi = k * pi
aliasi = j
pj = pj + (pi - 1/k)
if pj > 1/k
then largel = j; l = l + 1
else smalls = j; s = s + 1
while s > 0 do s = s - 1; probssmalls = 1
while l > 0 do l = l - 1; probllargel = 1

```

FIGURE 2. Alias method setup procedure (from Vose [68])

and for each reflected direction,  $k$  incident directions,  $\{\Theta_{i,1}, \Theta_{i,2}, \dots, \Theta_{i,k}\}$ , for a total of  $jk$  samples. The samples each have a representative solid angle  $\Delta\omega_{i,n}$  and a representative projected solid angle  $\Delta\Omega_{i,n}$  corresponding to  $\Theta_{i,n}$ , where  $1 \leq n \leq k$ .

The continuous p.d.f of (2.14) then becomes the p.m.f.,  $g'_{\Theta_i}$ :

$$\begin{aligned}
 g'_{\Theta_i}(\Theta_{i,n}; \Theta_{r,m}) &= \int_{\Delta\Omega_{i,n}} f_{\Theta_i}(\Theta_i; \Theta_{r,m}) d\Omega_i \\
 &\approx f_{\Theta_i}(\Theta_{i,n}; \Theta_{r,m}) \Delta\Omega_{i,n}
 \end{aligned}$$

where  $1 \leq m \leq j$  and  $1 \leq n \leq k$ . The approximation is valid for sufficiently small  $\Delta\Omega_{i,n}$  and will be used in generating the random variates in the following section. However, it does require a renormalization to ensure that the sum of the p.m.f. is 1. The

renormalized p.m.f. is

$$\begin{aligned}
 g_{\Theta_i}(\Theta_{i,n}; \Theta_{r,m}) &= \frac{f_{\Theta_i}(\Theta_i; \Theta_{r,m}) \Delta\Omega_{i,n}}{\sum_{a=1}^k f_{\Theta_i}(\Theta_{i,a}; \Theta_{r,m}) \Delta\Omega_{i,a}} \\
 &= \frac{\rho_s(\Theta_{i,n}; \Theta_r) \Delta\Omega_{i,n}}{\sum_{a=1}^k \rho_s(\Theta_{i,a}; \Theta_r) \Delta\Omega_{i,a}} \tag{2.24}
 \end{aligned}$$

We are now ready to define the lists from (2.18) and (2.19) required to generate random variates of the discretely sampled BRDF. For generating random variates of the incident directions corresponding to reflected direction  $\Theta_{r,m}$  use

$$X = \{\Theta_{i,1}, \Theta_{i,2}, \dots, \Theta_{i,k}\}$$

and

$$P = \{g_{\Theta_i}(\Theta_{i,1}; \Theta_{r,m}), g_{\Theta_i}(\Theta_{i,2}; \Theta_{r,m}), \dots, g_{\Theta_i}(\Theta_{i,k}; \Theta_{r,m})\}$$

### iBRDF

A new shader<sup>2</sup> was built for Radiance using the alias method described in the last section. This provides a means for discretized versions of arbitrary isotropic BRDFs to be used in the creation of synthetic images.

Uniform sampling is used to discretize the BRDF. The BRDF is separated into M, N, and R divisions of the reflected  $\theta$ , and incident  $\theta$  and  $\phi$  respectively. Since the BRDF is isotropic we define the coordinate system so that  $\phi_r = 0$ .

Notice that only half of the incident hemisphere need be sampled. The isotropic

---

<sup>2</sup>Radiance uses the term material type rather than shader.

nature of the sampled BRDF allows for translation in the azimuthal coordinates:

$$\rho(\theta_i, \phi_i; \theta_r, \phi_r) = \rho(\theta_i, \phi_i + \Delta\phi; \theta_r, \phi_r + \Delta\phi). \quad (2.25)$$

Also, a general property of the BRDF is the Helmholtz principle of reciprocity<sup>3</sup> [50]:

$$\rho(\theta_i, \phi_i; \theta_r, \phi_r) = \rho(\theta_r, \phi_r; \theta_i, \phi_i).$$

Combining these and the modulo nature of the azimuthal coordinate ( $\phi = \phi \bmod 2\pi$ ) gives

$$\begin{aligned} \rho(\theta_i, \phi_i; \theta_r, 0) &= \rho(\theta_i, \phi_i; \theta_r, 2\pi) \\ &= \rho(\theta_r, 2\pi; \theta_i, \phi_i). \\ &= \rho(\theta_r, 2\pi - \phi_i; \theta_i, 0) \end{aligned}$$

So we can limit the BRDF to the domain of  $\phi_i \in [0, \pi]$  by using

$$\rho(\theta_i, \phi_i; \theta_r, 0) = \begin{cases} \rho(\theta_i, \phi_i; \theta_r, 0) & \text{if } 0 \leq \phi_i \leq \pi, \\ \rho(\theta_r, 2\pi - \phi_i; \theta_i, 0) & \text{if } \pi < \phi_i < 2\pi. \end{cases}$$

The iBRDF data is accessible via two different functions. The first is a direct lookup of the BRDF values given incident and reflected directions. For this function, tri-linear interpolation is used to interpolate between the three sampled axes. The second

---

<sup>3</sup>It is commonly assumed that the principle of reciprocity for BRDFs always holds, but under certain condition reciprocity fails[64, 66]. However, for the discussion of this thesis it will be assumed that the BRDFs considered are fully reciprocal.

function creates random variates distributed as  $g_{\Theta_i}$  in (2.24) using the alias method. Interpolation is performed using a stochastic version of linear interpolation for both the selection of the sampled  $\phi_r$  and the selection of the incident direction within the selected  $\Delta\omega_i$ .

The above two functions provide the required BRDF information for the first and last integrals of (2.7). However, to accurately track the ambient illumination in the scene (using the second integral), Radiance also requires the diffuse reflectance. This is easily obtained by finding the minimum reflectance value of the BRDF and using this as the diffuse reflectance  $\rho_d$ . The specular reflectance used in the alias method is the difference

$$\rho_s(\Theta_i; \Theta_r) = \rho_s(\Theta_i; \Theta_r) - \rho,$$

since selection of random variates is driven only by the specular portion of the BRDF.

The spectral characteristics of the BRDF are captured by using three iBRDF data sets, one for each of the three axes of RGB space. Separate iBRDF functions are required because an arbitrary BRDF does not guarantee any spatial correlation between wavelengths. This assumption of BRDF correlation is made by the NEF database, discussed in the next chapter. The iBRDF data used as input is assumed to accurately represent the spectral domain.

Because of the uniform sampling used to discretize the BRDF, there is a limit to the highest spatial frequency which can be represented by iBRDF. Attempting to use a BRDF with spatial frequency beyond the limitation of the sampling density causes noticeable aliasing. The obvious solution is to perform adaptive sampling. This is left as future work.

## CHAPTER III

### RENDERING WITH NEFDS

In order to create a synthetic image of a real world surface using the Monte Carlo shader presented in the last chapter, the BRDF of the surface is required. Sampling the light reflection properties of the surface in all necessary directions,  $\Theta_i$  and  $\Theta_r$ , is possible, but it is a time consuming and expensive process. A more realistic approach is to represent the BRDF with an analytical function which itself can be sampled. The Nonconventional Exploitation Factors (NEF) is system which produces such analytical BRDFs, capable of representing real world surfaces.

The NEF data system (NEFDS) adds to the NEF a database of hundreds of pre-measured, physically based BRDFs. NEFDS has been used in the area of remote sensing and other areas of scientific research which require physically accurate surface reflection models. Making such a system available for use in computer graphics offers a wealth of new surfaces to synthetic image creation. Also, due to its physically accurate model, it offers a chance to validate the rendering system on which it is utilized.

In this chapter the NEFDS and its underlying reflection model are presented. Next, examples of specific BRDFs from the NEFDS are examined. Lastly the process required to render images using the NEFDS with iBRDF is detailed and the resulting images are shown.



### NEF Reflection Model

Over the past fifty years, a wide variety of analytical reflection models have been created to represent BRDFs. Shirley [62], Ellis [22], and especially Walker [72] offer thorough discussions of many light reflection models that have been proposed. Analytical models usually are defined with a number of functional parameters which reshape the BRDF. Some reflection models such as the Lambertian [41] or Phong [53] models are describable with only a few parameters. Offering fewer parameters necessarily allows the model to represent fewer BRDFs, but in exchange it is more difficult to do the wrong thing. Models such as the Beard-Maxwell [45], used as the basis of the NEF model presented in this section, or the He-Torrance [29] use many more functional parameters and have the potential to represent a vast number of BRDFs, but they also present the possibility of creating physically implausible BRDFs.

The solution offered by the Beard-Maxwell model is to build the function around the measurement process. The idea is similar to that used by Ward [43] in which Gaussian were fit curves to measured data, but Ward's implementation is slightly more ad-hoc. The Beard-Maxwell model uses very specific measurements at key directions and polarizations to fill in the necessary data. The model can then be verified with additional BRDF measurements to ensure that the surface being sampled is faithfully represented by the model with the selected parameters.

#### Beard-Maxwell

The Beard-Maxwell model presented by Maxwell et al. [45] is built on the assumption that the surface is a three dimensional terrain of micro-facets of varying orientation. In this model, reflected light is the result of only two physical occurrences. Light

is reflected off one of the micro-facets (first surface reflectance) and light is scattered out of the surface after having first entered the sub-surface medium (volumetric reflectance). The Beard-Maxwell reflectance model thus takes the form

$$\rho(\Theta_i; \Theta_r) = \rho_{fs}(\Theta_i; \Theta_r) + \rho_{vol}(\Theta_i; \Theta_r) \quad (3.1)$$

where  $\rho_{fs}$  and  $\rho_{vol}$  are the first surface and volumetric reflectance functions respectively. As in the last chapter, for the sake of notational clarity the wavelength of this wavelength dependent reflectance function is not listed as an explicit parameter. We will use this same liberty to hide other functional parameters which are tangential to current discussions.

As can be seen in Figure 3, first surface reflection causes light to be reflected in the specular direction (i.e., mirror reflection) off each individual micro-facet as determined by the micro-facet's normal,  $\hat{n}$ , not the overall surface normal,  $\hat{N}$ . Consequently, if light incident from direction  $\Theta_i$  is reflected by the first surface into the direction  $\Theta_r$ , there must be micro-facets with normals oriented near the half angle vector,  $\hat{H}$ . As shown in Figure 4,  $\hat{H}$  is the vector midway between the incident and reflected directions, calculated by:

$$\hat{N} \approx \hat{H} = \frac{\Theta_i + \Theta_r}{|\Theta_i + \Theta_r|}. \quad (3.2)$$

So the distribution of the first surface reflectance is determined by the distribution of the micro-facet normals which in turn is driven by the density function  $\Xi(\Theta)$ , the relative density of micro-facet normals (per steradian) in direction  $\Theta$ . Maxwell et al. calculated

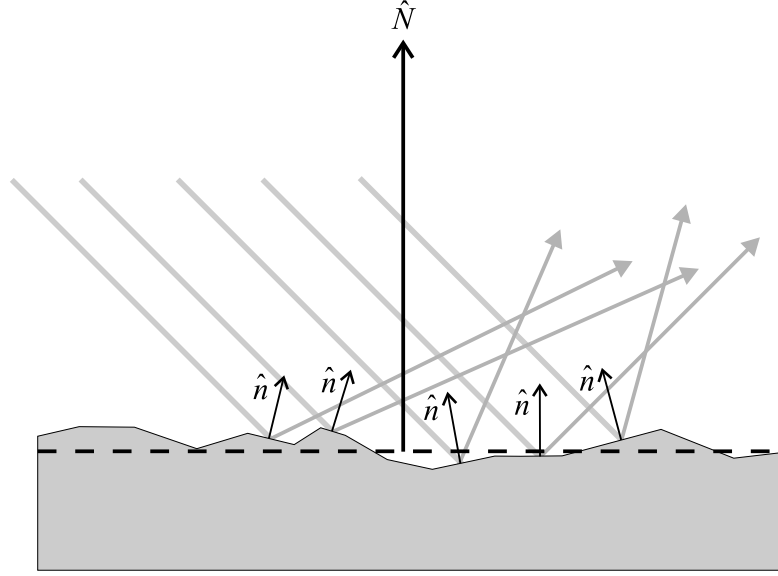


FIGURE 3. First surface reflection off micro-facets. A cross-section of the 3-dimensional surface terrain shows the specularly reflecting micro-facets and the macro-surface (shown as dashed line). The direction of first surface reflected light is determined by the facet normals,  $\hat{n}$ , rather than the macro-surface normal,  $\hat{N}$ .

the first surface reflectance to be

$$\rho_{fs}(\Theta_i, \Theta_r) = \frac{R(\beta)\Xi(\hat{H})}{4 \cos \theta(\Theta_i) \cos \theta(\Theta_r)} \text{SO} \quad (3.3)$$

where  $\beta$  is the bistatic angle,  $R(\theta)$  is the Fresnel reflectance and SO is a shadowing and obscuration term. The Fresnel reflectance term is due to the assumption that light reflecting off the micro-facets obeys the laws of Fresnel reflectance [30].

The shadowing and obscuration term, SO, accounts for the height distribution of the micro-facets. Shadowing and obscuration are due to intersection with other surface facets by the incident and reflected light rays respectively. Torrance and Sparrow [65] accounted for this with a purely analytical function derived from theory. Blinn [11] and Cook [17], who were the first to introduce shadowing and obscuration in computer

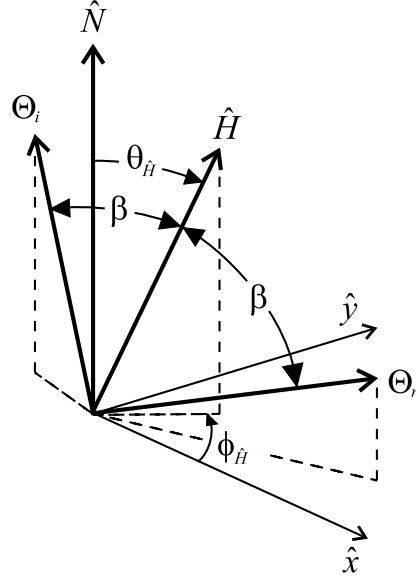


FIGURE 4. Half angle geometry

graphics, also used a purely analytical function. Beard and Maxwell chose to create their function based on empirical data:

$$\text{SO} = \frac{1 + \frac{\theta_{\hat{H}}}{\Omega} e^{-2\beta/\tau}}{1 + \frac{\theta_{\hat{H}}}{\Omega}} \left( \frac{1}{1 + \frac{\phi_n \theta_i}{\Omega \Omega}} \right) \quad (3.4)$$

where  $\Omega$  and  $\tau$  are parameters fit to the measured data and  $\phi_n$  is computed from geometry.

Rather than attempting to measure  $\Xi$  of (3.3) directly, Maxwell et al. cleverly replaced it with the measured zero-bistatic ( $\beta = 0$ ), first surface reflectance at the half angle,  $\rho_{fs}(\hat{H}, \hat{H})$ , using (3.3) rewritten as

$$\Xi(\hat{H}) = \frac{4\rho_{fs}(\hat{H}, \hat{H}) \cos^2 \theta_{\hat{H}}}{R(0)}. \quad (3.5)$$

(Note that  $SO = 1$  when  $\beta = 0$ .) Substituting (3.5) back into (3.3) gives

$$\rho_{fs}(\Theta_i, \Theta_r) = \frac{R(\beta)}{R(0)} \frac{\rho_{fs}(\hat{H}, \hat{H}) \cos^2 \theta_{\hat{H}}}{\cos \theta(\Theta_i) \cos \theta(\Theta_r)} SO. \quad (3.6)$$

So by measuring the zero-bistatic, first surface reflectances, all first surface reflectances can be calculated. This is simplified even further by their assumption that the surface is isotropic. This assumption allows us to use (2.25) to rewrite (3.6) as

$$\rho_{fs}(\Theta_i, \Theta_r) = \frac{R(\beta)}{R(0)} \frac{\rho_{fs}(\theta_{\hat{H}}, 0; \theta_{\hat{H}}, 0) \cos^2 \theta_{\hat{H}}}{\cos \theta(\Theta_i) \cos \theta(\Theta_r)} SO. \quad (3.7)$$

In order to generate reflectance values for all incident and reflected directions, we need only to sample  $\rho_{fs}(\theta_{\hat{H}}, 0; \theta_{\hat{H}}, 0)$  for  $\theta_{\hat{H}}$  between 0 and 90 degrees.

In practice, (3.7) requires two modifications. The first is a consequence of not being able to measure directly the zero-bistatic reflectance (it would require the source and receiver to be coaxial). Instead the near zero-bistatic ( $\beta \approx 3$  degrees) reflectance is measured and from this the zero-bistatic reflectance is calculated. Solving (3.7) for the zero-bistatic reflectance gives

$$\rho(\theta_{\hat{H}}, 0; \theta_{\hat{H}}, 0) = \frac{R(0)}{R(\beta)} \frac{\cos \theta(\Theta_i) \cos \theta(\Theta_r)}{\rho(\Theta_i, \Theta_r) \cos^2 \theta_{\hat{H}}} \frac{1}{SO}. \quad (3.8)$$

So the zero-bistatic reflectance can be found by evaluating (3.8) using near zero-bistatic directions  $\Theta_i$  and  $\Theta_r$ .

The second modification required of (3.7) is due to the origin of the measured light reflectance. As shown in (3.1), the measured reflectance is the sum of both the first surface and the volumetric components. Somehow the first surface reflectance must

be extracted out of the measured reflectance to obtain the zero-bistatic first surface reflectance required in (3.7).

Maxwell et al. performed this separation by making the assumptions that any light reflected from the first surface maintains its original polarization (i.e., incident and reflected light are of like polarization) and any light reflected through volumetric scattering is totally depolarized. Given the two polarizations  $\alpha_1 \neq \alpha_2$ , these two assumptions can be summarized by the two equations<sup>1</sup>

$$\rho_{\alpha_1\alpha_2,fs} = 0 \quad (3.9)$$

and

$$\rho_{\alpha_1\alpha_1,vol} = \rho_{\alpha_1\alpha_2,vol}. \quad (3.10)$$

The cross polarized version of (3.1) is

$$\rho_{\alpha_1\alpha_2} = \rho_{\alpha_1\alpha_2,fs} + \rho_{\alpha_1\alpha_2,vol}$$

which when combined with (3.9) and (3.10) results in

$$\begin{aligned} \rho_{\alpha_1\alpha_2} &= 0 + \rho_{\alpha_1\alpha_1,vol} \\ &= \rho_{\alpha_1\alpha_1,vol}. \end{aligned} \quad (3.11)$$

---

<sup>1</sup>We follow the same notation as in Maxwell et al. [45] to denote polarized reflectance by  $\rho_{\alpha_i\alpha_r}$ , where the positions of  $\alpha_i$  and  $\alpha_r$  indicate the polarization of the incident and reflected light respectively. The polarization state of the incident light is either parallel ( $\parallel$ ) or perpendicular ( $\perp$ ) to the plane of incidence. The polarization state of the reflected light is described in the same way, but with respect to the reflectance plane.

Now using the like polarized version of (3.1) and applying (3.11) results in

$$\begin{aligned}
 \rho_{\alpha_1 \alpha_1} &= \rho_{\alpha_1 \alpha_1, f.s.} + \rho_{\alpha_1 \alpha_1, vol} \\
 &= \rho_{\alpha_1 \alpha_1, f.s.} + \rho_{\alpha_1 \alpha_2} \\
 \rho_{\alpha_1 \alpha_1, f.s.} &= \rho_{\alpha_1 \alpha_1} - \rho_{\alpha_1 \alpha_2}
 \end{aligned} \tag{3.12}$$

Finally, the first surface reflectance can be expressed in measurable quantities by applying (3.9) and (3.12) to the four possible combinations of polarization:

$$\begin{aligned}
 \rho_{f.s.} &= \rho_{\perp\perp, f.s.} + \rho_{\perp\parallel, f.s.} + \rho_{\parallel\perp, f.s.} + \rho_{\parallel\parallel, f.s.} \\
 &= \rho_{\perp\perp, f.s.} + 0 + 0 + \rho_{\parallel\parallel, f.s.} \\
 &= (\rho_{\perp\perp} - \rho_{\perp\parallel}) + (\rho_{\parallel\parallel} - \rho_{\parallel\perp}).
 \end{aligned} \tag{3.13}$$

Similarly, the volumetric reflectance can be expressed in measurable quantities by applying (3.10) and (3.11) to the four possible combinations of polarization:

$$\begin{aligned}
 \rho_{vol} &= \rho_{\perp\perp, vol} + \rho_{\perp\parallel, vol} + \rho_{\parallel\perp, vol} + \rho_{\parallel\parallel, vol} \\
 &= \rho_{\perp\parallel, vol} + \rho_{\perp\parallel, vol} + \rho_{\parallel\perp, vol} + \rho_{\parallel\perp, vol} \\
 &= 2\rho_{\perp\parallel, vol} + 2\rho_{\parallel\perp, vol} \\
 &= 2\rho_{\perp\parallel} + 2\rho_{\parallel\perp}
 \end{aligned} \tag{3.14}$$

The volumetric reflectance of (3.1),  $\rho_D$  is represented by either Lambertian re-

flectance or directional diffuse reflectance,  $\rho_{diff}$ :

$$\rho_{vol} = \begin{cases} \rho_D \\ \rho_{diff} = \frac{2\rho_v f(\beta)g(\theta_{\hat{N}})}{\cos \theta_i + \cos \theta_r} \end{cases} \quad (3.15)$$

where  $f(\beta)$  and  $g(\theta_{\hat{N}})$  are empirically determined. The directional diffuse component accounts for any subsurface directional scattering and is selected only if there is any directional reflection unaccounted for by the first surface reflectance. The Lambertian reflectance is selected if the first surface reflectance accounts for all directional reflectance. The directional diffuse component of (3.15) is based on a model of a subsurface of finite thickness built on a reflective base. It may be more appropriate to model subsurface as having infinite thickness in which case the volumetric reflectance simplifies to

$$\rho_{vol} = \begin{cases} \rho_D \\ \rho_{diff} = \frac{2\rho_v}{\cos \theta_i + \cos \theta_r} \end{cases} \quad (3.16)$$

#### Modification to Beard Maxwell

The NEF uses a modified form of the Beard-Maxwell reflection model to characterize the reflection properties of surfaces in the NEF database. The NEF Beard-Maxwell (NEF-BM) model includes changes in the attempt to more accurately represent surfaces other than paint, the original target of the Beard-Maxwell model. Additionally, fixed measurements are introduced which can be used to determine appropriate values for the model's free parameters.

In the Beard-Maxwell model, only one volumetric components was utilized, either the Lambertian reflectance or the directional diffuse reflectance. In the NEF-BM



model both are used. The volumetric Lambertian reflectance is referred to as simply diffuse reflectance and is attributed to multiple first surface reflections. The volumetric directional diffuse reflectance is itself referred to as volumetric reflectance,  $\rho_{vol}$ , and is attributed to all the reflectance due to subsurface light interaction.

The NEF-BM model uses a simplified form (3.4) for its shadowing and obscuration function:

$$SO = \frac{1 + \frac{\theta_{\hat{N}}}{\Omega} e^{-2\beta/\tau}}{1 + \frac{\theta_{\hat{N}}}{\Omega}}.$$

The model also uses the simplified form of directional subsurface scattering from (3.16).

So the complete NEF-BM BRDF can be written

$$\begin{aligned} \rho(\Theta_i; \Theta_r) = & \frac{R(\beta)}{R(0)} \frac{\rho_{fs}(\theta_{\hat{H}}, 0; \theta_{\hat{H}}, 0) \cos^2 \theta_{\hat{H}}}{\cos \theta_i \cos \theta_r} \left( \frac{1 + \frac{\theta_{\hat{H}}}{\Omega} e^{-2\beta/\tau}}{1 + \frac{\theta_{\hat{H}}}{\Omega}} \right) + \\ & \rho_D + \frac{2\rho_v}{\cos \theta_i + \cos \theta_r} \end{aligned} \quad (3.17)$$

As in the BM model, the NEF-BM performs the zero-bistatic BRDF measurements at all four combinations of polarization using (3.13) and (3.14) to generate the first surface reflection parameters as well as the diffuse and volumetric coefficients. Additionally the NEF-BM performs two other series of measurements.

The first is a series of specular BRDF measurements for parallel polarized source and receiver over  $10 \text{ deg} \leq \theta_i \leq 80 \text{ deg}$  with  $\phi_i = 0 \text{ deg}$  and  $\phi_r = 180 \text{ deg}$ . For each sampled incident direction, the receiver direction is varied about the mirror direction in the plane of incidence by  $\theta_i - 5 \text{ deg} \leq \theta_r \leq \theta_i + 5 \text{ deg}$ . Data obtained from these measurements provides a means of calculating the complex index of refraction components,  $n$  and  $k$  which are required for computing the Fresnel reflection coefficient,  $R$ .

The second series of measurements uses a fixed source direction and varying re-

ceiver direction, in the plane of incidence over  $-90 \text{ deg} \leq \theta_r \leq 90 \text{ deg}$ . These measurements offer means to select the shadowing and obscuration parameters,  $\tau$  and  $\Omega$ . These measurements also provided data for verification of the selected model parameters.

### Limitations of the Model

These measurements hopefully generate a reflection model which faithfully represents the actual reflection behavior of the target surface. However, a model is an approximation; there are limitations to the types of BRDFs it can accurately represent. Some surface BRDFs simply cannot be accurately approximated with the NEF-BM model using any combination of parameter values. For a model which was initially constructed to represent simple paint reflection, it covers a broad range quite accurately, but care must be used in applying it to new BRDFs.

Another limitation of the NEF Beard-Maxwell model is its inaccuracy at grazing angles. The model was created primarily for remote sensing<sup>2</sup> which involves interpreting imaged data from aircraft or satellites, so accuracy at grazing angles was not a large concern. For use in computer graphics however, grazing angles are to be expected in every scene.

The problem lies in the fact that the NEF-BM BRDF of (3.17) at grazing incidence,  $\Theta_{gi}$  integrated over the reflected hemisphere results in values greater than one:

$$\begin{aligned} \int_{\Omega_r} \rho(\Theta_{gi}; \Theta_r) d\Omega_r &= \int_{\Omega_r} \rho_{fs}(\Theta_{gi}; \Theta_r) d\Omega_r + \int_{\Omega_r} \rho_D d\Omega_r + \int_{\Omega_r} \frac{2\rho_v}{\cos \theta_{gi} + \cos \theta_r} d\Omega_r \\ &= 1 + \pi\rho_D + 4\pi\rho_v \end{aligned}$$

---

<sup>2</sup>The Remote Sensing Tutorial [63] offers a thorough history and overview of this field of study.

Consequently light incident at grazing angles will result in more energy reflected than was incident. In practice this has not been a problem mainly because of the foreshortening of incident energy at grazing angles. For the long term acceptance of the Beard-Maxwell model, this shortcoming should be addressed.

### NEFDS

The NEFDS allows those working in the area of remote sensing to perform complex radiometric calculations taking into consideration the properties of the target material, the material background, the measuring sensors, and the atmospheric environment. At the heart of this system, and of particular interest to this thesis, is the BRDF database. This database contains the BRDFs of hundreds of surfaces from a dozen different categories. In this section, we will present a discussion of the BRDFs available and offer an overview of the relevant portions of the NEFDS.

#### Available Material Types

There are currently over 400 materials available in the NEFDS. These materials correspond to a wide variety of objects ranging from dirt to tree canopies. The materials fall into 12 different categories: asphalt, brick, camouflage, composite, concrete, fabric, water, metal, paint, rubber, soil and wood.

Although the number of materials is large and the variety is wide, the selection is limited by two key conditions. One requirement for the inclusion of a material in the database is that the BRDF of the material must be well represented by the NEF-BM BRDF model. For example, the BRDF should not be characterized by extreme anisotropy since the NEF-BM BRDF model only works with isotropic data. (There

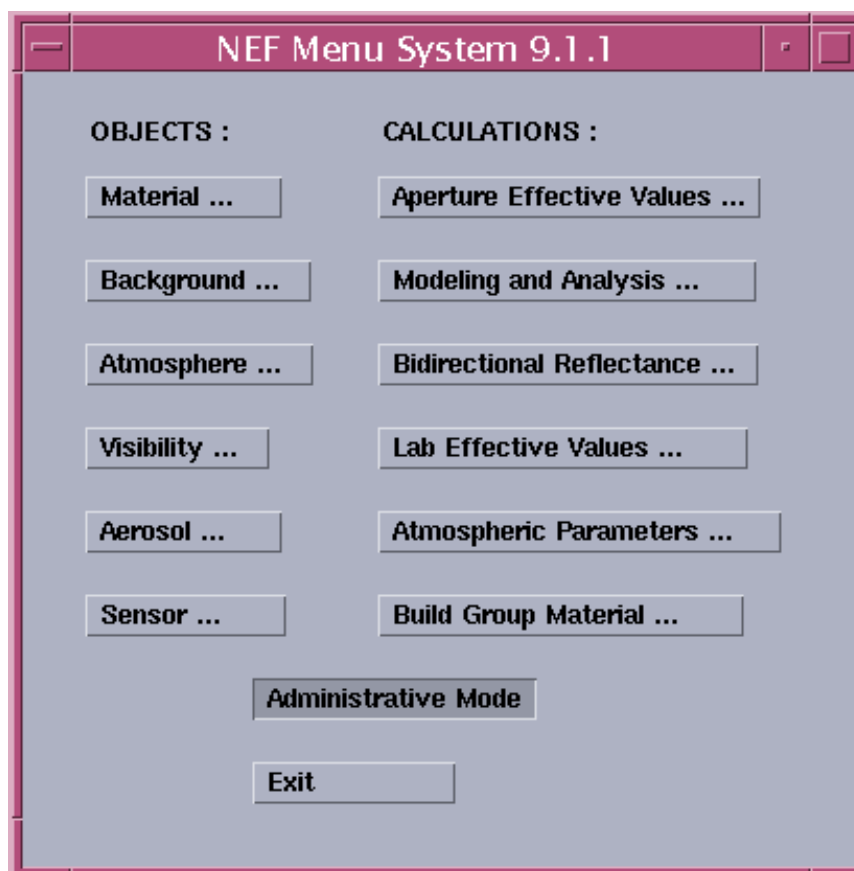
are in fact some materials included in the NEFDS which are anisotropic. To represent anisotropic material using the NEF-BM model, the material's BRDF is averaged to isotropy.)

The second condition is a result of the data's origin. As mentioned before, the main use of the NEFDS has been in the area of remote sensing. Because of this, the materials in the database were selected on the basis of applicability to that field of work. They include objects which would be viewed from a remote sensor (e.g., a satellite). This still offers a potential wealth of BRDF data for use in computer graphics but is currently constrained to this one area. This however does not restrict future measurement and inclusion of other materials having more direct applicability to computer graphics.

#### Interactive Use - *NefMenu*

The primary method of interacting with NEFDS is through the XWindows graphical user interface (GUI) provided by the program *NefMenu*. This offers control over all available programs and administrator functions. Figure 5 shows the main menu of *NefMenu* (being run in administrator mode). A discussion of the capability of *NefMenu* is well beyond the scope of this thesis (see the NEF Users Guide for detailed discussion of *NefMenu* [49]), instead a brief overview of some of the functionality related to the BRDF will be given.

From the main menu, materials or groups of materials can be analyzed using the various available tools. Selecting *Material...* produces the *Material Selection* window shown in Figure 6. The individual materials are available through the *All Materials* entry, while the group materials (i.e., values averaged across similar materials) are entries themselves.

FIGURE 5. Main menu of *NefMenu*

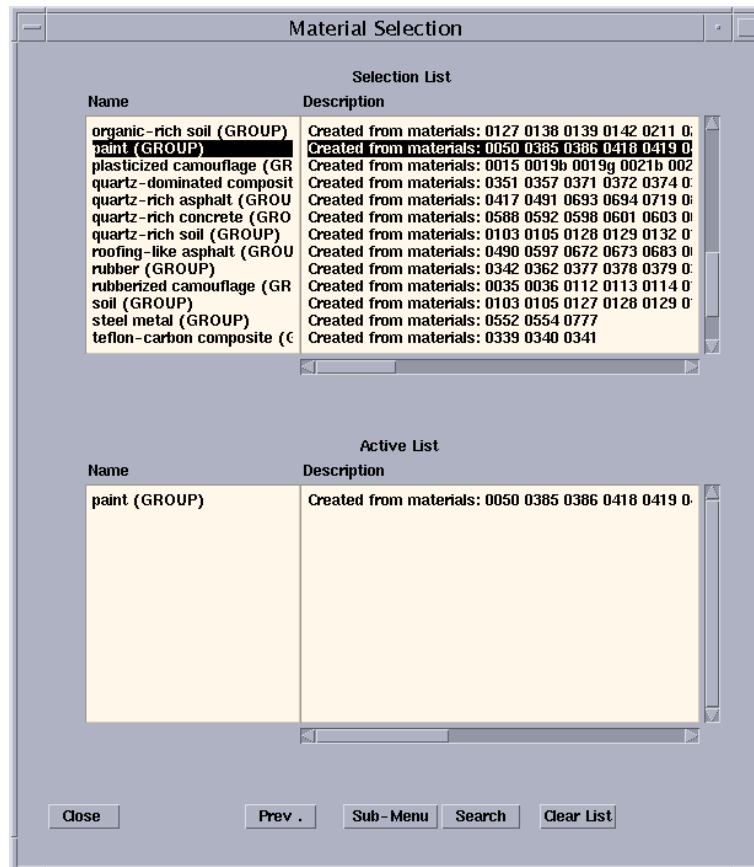


FIGURE 6. Material Selection menu of *NefMenu*

**BRDF Parameters**

Object Name: 0880UUUPNT 444

Lambda : 0.325

N : 1.54    K : 0.194    Rho XI : 0.00103

Rho XZ : 0.00103    Rho V : 0.00047    SIGMA : 0.196

DHR : 1    RO : -777    TAU : 9.37

OMEGA : 58.3    BIAS : 0.0411    Q2 : -777

DP0 : -777    DP90 : -777

F(BETA) : -777    -777    -777    -777    -777

G(THETA) : -777    -777    -777    -777    -777

F(BETA) : -777    -777    -777    -777    -777

G(THETA) : -777    -777    -777    -777    -777

Variance	N	K	RhoXI	RhoV	Tau	Omega	Sigma	Bias
N	0.000905	.00335	0	0	0	0	0	0
K	-0.00335	0.0135	0	0	0	0	0	0
RhoXI	0	0	.00194	0.0032	0	0	0	0
RhoV	0	0	0.0032	0.0164	0	0	0	0
Tau	0	0	0	0	.09e-07	.7e-08	0	0
Omega	0	0	0	0	.7e-08	.39e-08	0	0
Sigma	0	0	0	0	0	0	.95e-05	.29e-05
Bias	0	0	0	0	0	0	.29e-05	.43e-05

Close    Page    Next    Print    Store

FIGURE 7. BRDF Parameters menu of *NefMenu*, page 1

The low level material data used to generate the BRDF can be viewed directly as shown in Figures 7 and 8. This material data, found in the .mat and .grp files, contains hundreds of entries so using such a viewer with fully titled and organized fields offers a great advantage over sampling the data files themselves. (The Nonconventional Exploitation Factors Data System (NEFDS) Specifications [48] provides a detailed discussion of the underlying data structure used to generate the NEF-BM BRDF.)

The spectral reflectance function of any of the materials or material groups can be shown graphically. This is the hemisphere reflectance for incident light normal to the

**BRDF Parameters**

Object Name: 0880UUUPNT 444

Lambda : 0.325

THETA N :	0	.07e+09	.07e+09	.07e+09	.07e+09	.07e+09
RHO' COS**2 :	0.0521	0.0522	0.0513	0.0499	0.0479	0.0457
THETA N :	.07e+09	.07e+09	.07e+09	.07e+09	.07e+09	.07e+09
RHO' COS**2 :	0.0432	0.0404	0.0374	0.0345	0.0315	0.0288
THETA N :	.07e+09	.07e+09	.07e+09	.07e+09	.07e+09	.07e+09
RHO' COS**2 :	0.0263	0.0238	0.0215	0.0194	0.0174	0.0158
THETA N :	.07e+09	.07e+09	.07e+09	.07e+09	.07e+09	.07e+09
RHO' COS**2 :	0.0142	0.0116	0.00958	0.00793	0.00667	0.00565
THETA N :	.07e+09	.07e+09	.07e+09	.07e+09	.07e+09	.07e+09
RHO' COS**2 :	0.00495	0.00419	0.00376	0.00339	0.00309	0.00281
THETA N :	.07e+09	.07e+09	.07e+09	.07e+09	.07e+09	.07e+09
RHO' COS**2 :	0.00257	0.0023	0.00213	0.00196	0.00177	0.00166
THETA N :	.07e+09	.07e+09	.07e+09	.07e+09	.07e+09	.07e+09
RHO' COS**2 :	0.00152	0.00138	0.00126	0.00116	0.00108	0.000947
THETA N :	.07e+09	.07e+09	.07e+09	.07e+09		
RHO' COS**2 :	0.000857	0.000759	0.000691	0		

FIGURE 8. BRDF Parameters menu of *NefMenu*, page 2



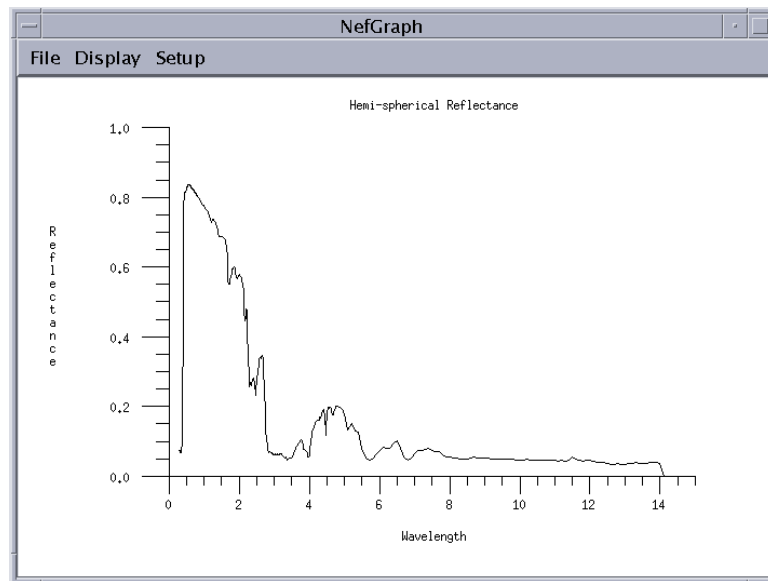


FIGURE 9. Spectral reflectance function for material 0880, yellow paint

surface at a particular wavelength:

$$R(\lambda) = \int_{\Omega_r} \rho(\Theta_{\hat{N}}; \Theta_r; \lambda) d\Omega_r$$

The spectral reflectance function of material number 0880, yellow paint, and material number 0221, red dirt, are displayed in Figures 9 and 10 respectively. Notice that the visible spectrum, which is generally accepted as ranging from  $.380\mu\text{m}$  through  $.770\mu\text{m}$ , is only a small fraction of the total displayed range. The spectral range utilized by the NEFDS ranges from the ultra violet to the far infra-red, another consequence of its design for remote sensing. The numeric spectral reflectance values used to create the spectral reflectance graphs may also be accessed directly as shown in Figure 11.

The NEFDS may be queried for BRDF values of materials or material groups at ranges of wavelengths for any given geometry. The window accepting the queried parameters, shown in Figure 12, requires the angles of the source, receiver and sample

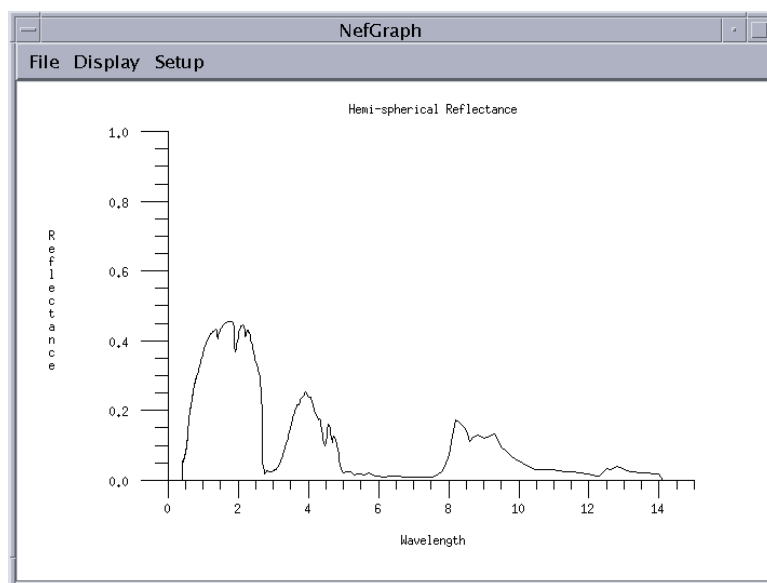


FIGURE 10. Spectral reflectance function for material 0221, red dirt

surface as well as the range of the wavelength of light. The required angles, measured in degrees, are the azimuthal and elevation (angle from horizon). The results shown in Figure 13 are the BRDF values calculated in increments of 2 nanometers.

### Standalone Programs

Often it is more convenient to use command line interface for program control. For this reason most of the NEFDS programs available through the XWindows interface are also available directly from the command line. The command line equivalency to Figure 12 is the program *BRDF* which takes as input the same six defining angles and the spectral range and returns the computed list of corresponding BRDF values. For example to find the reflectance of material number 0880, yellow paint, using parameters equivalent to those used in Figure 12, execute command shown in Figure 14. If all the parameters are not specified on the command line, *BRDF* will prompt the user for the

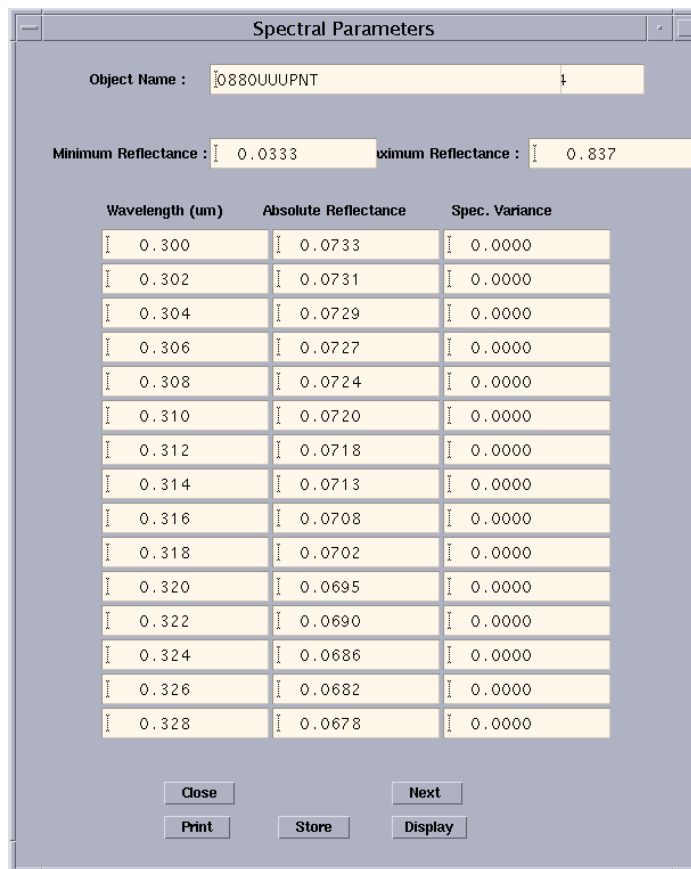


FIGURE 11. Raw Spectral Reflectance values for material 0880, yellow paint

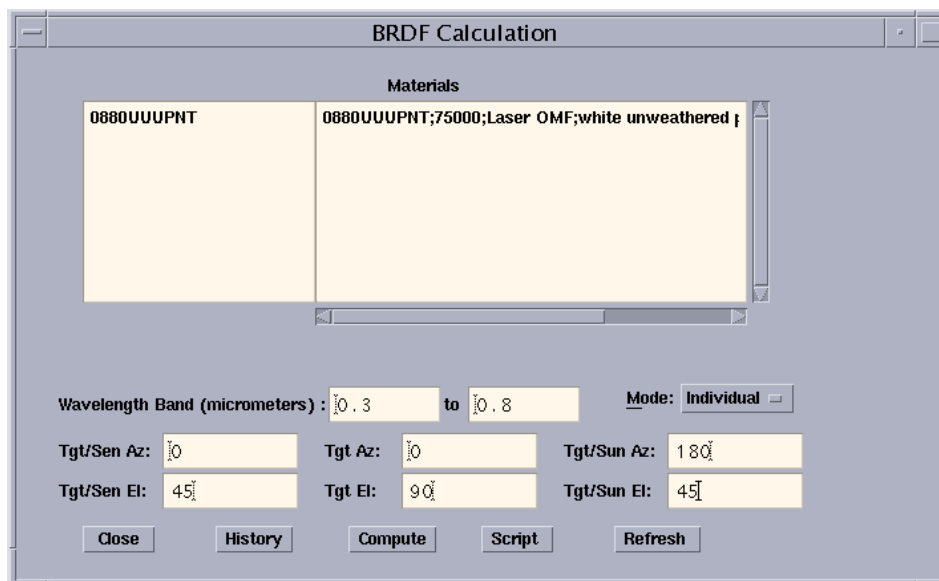


FIGURE 12. Spectral and spatial parameters used to generate Figure 13 for material 0880, yellow paint

required data, eliminating the need to remember the exact command syntax.

Using a program from the command line also offers the user the ability to run the command as part of a batch job. This is the method utilized by *nefquery*, the program used to generate the iBRDF data file. This program is discussed in more detail in the next section.

### Rendering Data

In this section the NEFDS is used to create data files of BRDFs. Using these data files, images are rendered of objects modeled with these sampled BRDFs. To render the images, we used the iBRDF extension to Radiance discussed in chapter II.



FIGURE 13. Spectral BRDF values for material 0880, yellow paint

```

> BRDF -M 0880UUUPNT -e 0 45 -i 180 45 -n 0 90 -w .3 .8
0880UUUPNT

Wavelength          RHO'
*****
0.3                 0.174236
0.302               0.173761
0.304               0.173286
0.306               0.17281
0.308               0.172097
0.31                0.171146
:

```

FIGURE 14. Command line request to *BRDF*

### Sampling Data for Use in iBRDF

The iBRDF shader requires a data file containing the BRDF values at specific angular combinations. A single NEFDS BRDF is calculated using the program *BRDF* as shown in the previous section. *brdfscript* was created to automate the data gathering process by generating a script file with all of the required calls to *BRDF*. The result of running the script file is a human readable list of all BRDF values and descriptions which must be parsed to be useful to iBRDF. *nefquery* was written to combine all these programs together. The input to *nefquery* is the material number and the output is the iBRDF data file.

A single call to *BRDF* requires network and server access resulting in an execution time of nearly one second. Consequently the total time required to create one iBRDF

data file (which typically contains on the order of 1 million samples) is about 10 hours. To speed this up *brdfscan*, a stand alone program duplicating the functionality of *BRDF* was written by Michael Metzler, the principal author the NEFDS. This program uses the same parameters as *BRDF* except for the material number, which is replaced with the material filename. By accessing the data files directly, rather than through the server, *brdfscan* allows the full iBRDF data file to be created in about one minute. Unfortunately the current version gives BRDF values which are slightly different than when run through NEFDS. The difference is not too significant, but the discrepancy should be addressed.

### Creating Images

Figure 15 is the rendered image of several objects modeled with different NEF BRDFs. Figures 16 and 17 show objects which have texture maps modified by the BRDFs of different NEF materials.



FIGURE 15. Vases with NEF materials (left to right) Bare Construction Lumber, Gloss Paint on Metal, and Scored Aluminum. Image from [72].



FIGURE 16. Vases with NEF materials Bare Construction Lumber, Gloss Paint on Metal, and Scored Aluminum. Image from [72].



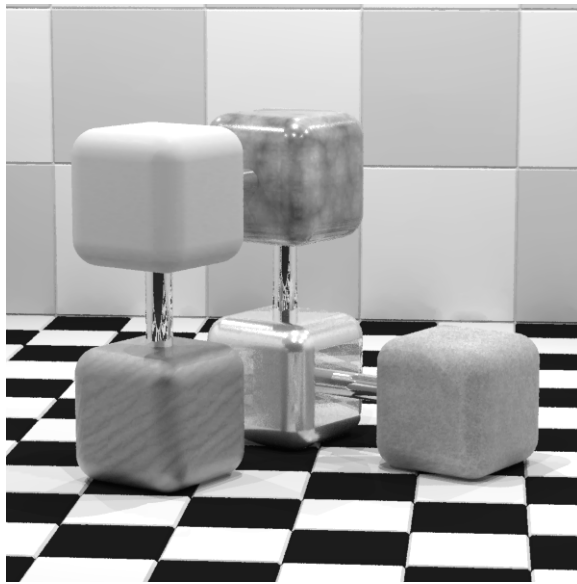


FIGURE 17. Cubes with NEF materials (top row) Cement, Gloss Paint on Metal, (bottom row) Bare Construction Lumber, Scored Aluminum, and Weathered Concrete. Image from [72].

## CHAPTER IV

### APPEARANCE BASED MEASUREMENTS

Of the many attributes which define an object's appearance, two of the most significant are color and gloss. From color alone we can determine the season by the leaves, the weather by the sky, and the freshness of meat sold in the market. Gloss reveals to us the age of a car, the cleanliness of a table, and the quality of sushi. It is no wonder then that to manufacturers, color and gloss are of paramount importance in ensuring the quality of a product's appearance. This chapter considers industry standards for measurement of color and gloss and how these standards can be applied to realistic image synthesis.

#### Subsurface Highlights - Flop

In computer graphics the color of an opaque dielectric is typically modeled with Lambertian reflectance; the color is considered constant with respect to the viewing angle. This correlates with the standard methods of color measurement used in industry which are based on the same Lambertian (or near Lambertian) reflectance [51, 9, 16]. These methods use the geometries 0/45, 45/0, 0/diffuse, or diffuse/0, with the first number specifying illumination angle and the second number specifying the detector angle. Measurement of color by a single detector angle is sufficient if there is relatively little angular variation in the object's color (e.g. this is the case with many scattering pigments). However, a single measurement is not sufficient for goniochromatic (color changes with angle) materials such as metallic and pearlescent paints.

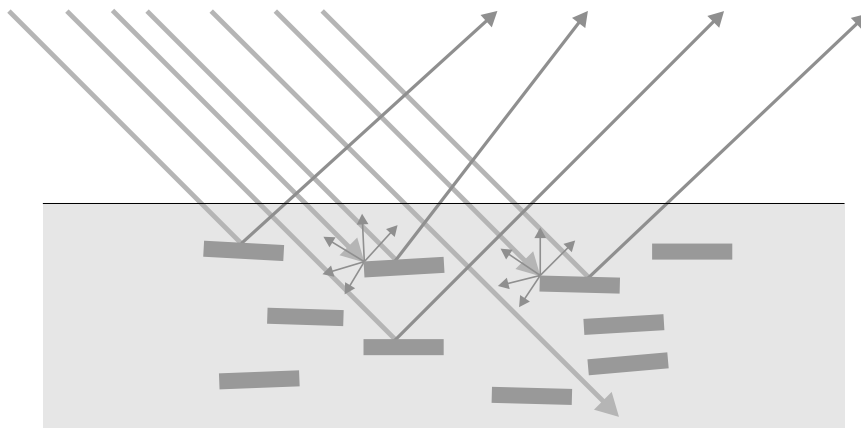


FIGURE 18. Subsurface structure of metallic paint (after Berns [9])

Metallic paints are produced by combining metallic platelets with colored particles or dyes in the paint substrate [10, 14]. As diagrammed in Figure 18, the platelets are oriented near parallel to the surface so that most of the light is reflected in the specular (i.e., mirror) direction while a small portion is scattered diffusely (due to edge scatter). The colored particles or dyes tint the light through selective absorption resulting in a bright color in the near specular direction falling off to a dark color far away from specular. This change in lightness, which is termed flop (also called flip/flop, two tone, or metallic travel) can be seen in Figure 24. A similar flop phenomenon is also achieved with pearlescent paint by using small flakes of mica coated with thin layers of metal oxide [10, 14, 25, 31] which both reflect and transmit incident light as shown in Figure 19. These thin layered platelets cause interference and thus the flop phenomena in pearlescents involves variation in all three coordinates of the color space rather than simply lightness [8].

As mentioned above, a single color measurement is insufficient to characterize the color of gonioapparent material. Much work has been done to determine the measurements required to characterize gonioapparent surfaces. Alman found that three angles

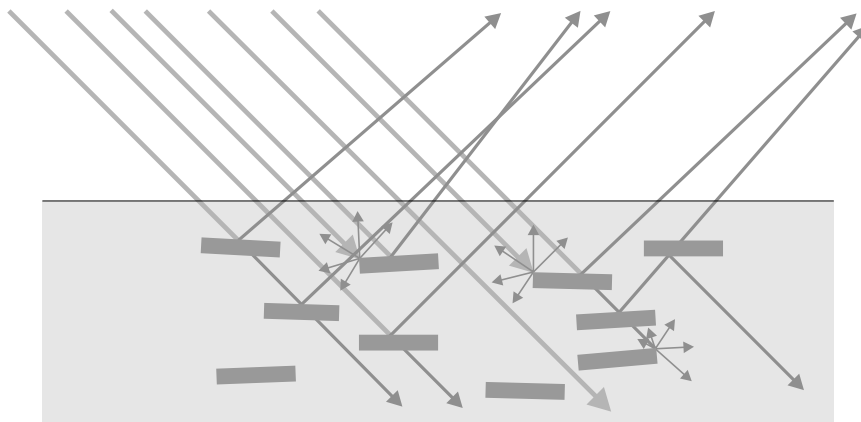


FIGURE 19. Subsurface structure of pearlescent paint (after Berns [9])

are sufficient for characterizing the flop of metallic paints [1]. The paints were illuminated at 45 degrees from normal and were measured at near the specular (15 degrees from specular), far from the specular (110 degrees) and one more measurement in between (45 degrees). Interpolation between these three measurements in CIELAB using a second degree polynomial was found to produce acceptable results. These results were again verified by Rodrigues [55]. Saris, et al. also determined that three similar angular measurements are sufficient for capturing the flop of metallic paints [61]. They compared instrumental measurements to human observation and found the best correlation at the angles 25, 45 and 110 degrees from specular with light incident at 45 down from normal. Venable used a more complex exponential based function to interpolate measured XYZ color data from metallic surfaces [67]. He also found that three measurement angles are sufficient to characterize flop and recommended using normal incident illumination measured at 20, 40 and 75 degrees from specular. Interpolation of measured data may also be possible by fitting the data to theoretical models. For example, Bridgeman used radiative heat transfer theory to predict reflection from metallic paint [13]. Additional discussions and comparisons of various metallic paint measurement methods of

metallic paints have been presented by Rodrigues [56] and McCamy [46].

Although no standards have as yet been specified, the measurement angles of existing instruments utilized in industry will probably dictate standards. Currently there are working groups in both the American Society for Testing and Materials (ASTM) (sub-committee E12.12, Metallic and Pearlescent Colors) and the Deutsches Institut für Normung (DIN) which are in the process of discussing final specifications for standard measurements of goniochromatic surfaces [57]. It appears that the ASTM group will accept the DuPont (i.e., Alman) angles of 15, 45 and 110 degrees while the DIN will likely use 25, 45 and 75 degrees [9, 58]. The three required angles of measurement have been assigned the terms near-specular, face, and flop corresponding to the increasing aspecular angles of the three measurements [5]. Common to both of the proposed standards is the sufficiency of three angles of measurement and the use of the 0/45 measurement (previously existing in CIE color measurement standards) for the face measurement.

Pearlescent and other effects paints present more difficulty because of the additional angular dependency of chroma and hue as well as lightness. Rodrigues showed that the original Alman model can be used to measure and interpolate  $a^*$  and  $b^*$  values in addition to  $L^*$  values using CIELAB [55]. Rösler used illumination at four angles from specular but also allowed for surface tilt in three positions to provide a total of twelve aspecular angles [59]. He found that for many surfaces (e.g. metallics) three or four measurements are sufficient. However for more complex interference and effects surfaces, Rösler emphasized that more measurement angles are possibly required. Another ASTM sub-committee (E12.14, Multidimensional Characterization of Appearance) is interested in developing instrumental and visual standards for multidimensional goniochromatic surfaces. Results from this group are still pending.

## Utilizing Color in Computer Graphics

The equation which dictates the color of a surface in realistic image synthesis is the BRDF. As mentioned before, the BRDF is the ratio of differential radiance to differential irradiance for a given incident and reflected direction at a given frequency of light:

$$\rho(\Theta_i; \Theta_r; \lambda) = \frac{dL(\Theta_i; \Theta_r; \lambda)}{dE(\Theta_i; \lambda)}. \quad (4.1)$$

The scale of this ratio generally determines a color's lightness while hue and saturation are the result of the BRDF's variance with respect to the wavelength of light.

Rather than tracking the BRDF across the full spectrum of light, most image synthesis is performed using the corresponding tristimulus values. Even with this reduction in spectral information, it is still possible to produce colorimetrically correct images, given certain stipulations. Figure 20 shows the normal propagation of spectrally dependent source energy from direction  $\Theta_i$ , reflecting off the material  $M_1$  toward an observer in direction  $\Theta_r$ . The spectrally dependent radiance seen by the observer is the product of the spectrally dependent irradiance and the material's spectrally dependent reflectance.

Accepting some limitations to be described later, the system in Figure 20 can be replaced by an equivalent situation. In the alternative scheme, an equivalent exitant radiance is achieved by both using an irradiance with a suitable constant value at all wavelengths and by setting the reflectance  $\rho_2$  of the material to be proportional to the product  $I_1\rho_1$  (Figure 21). Thus the observer,  $O_2$  sees the same energy distribution as seen by  $O_1$  even though the distributions were produced by different means.

Using standard CIE methods, CIEXYZ tristimulus values corresponding to the observed radiance can be calculated. If the coordinate transformation between CIEXYZ and a specific RGB system is known, the equivalent RGB values can also be determined

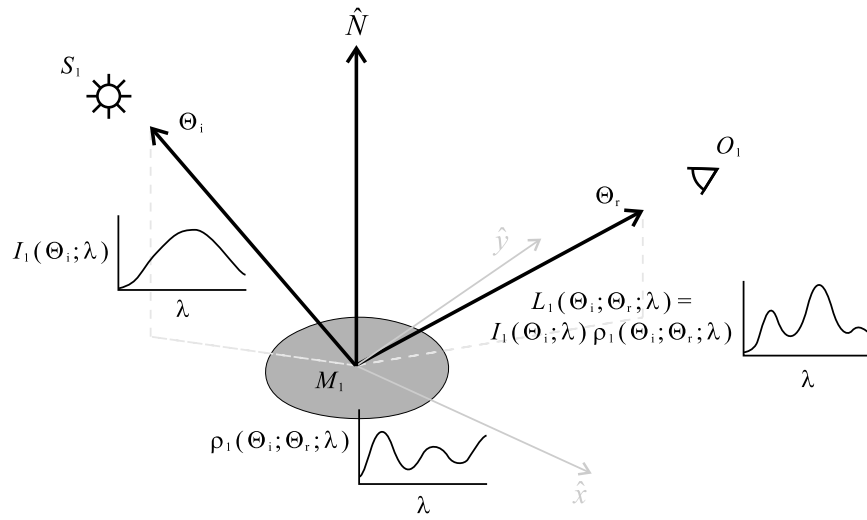


FIGURE 20. Observed radiance using full spectral method

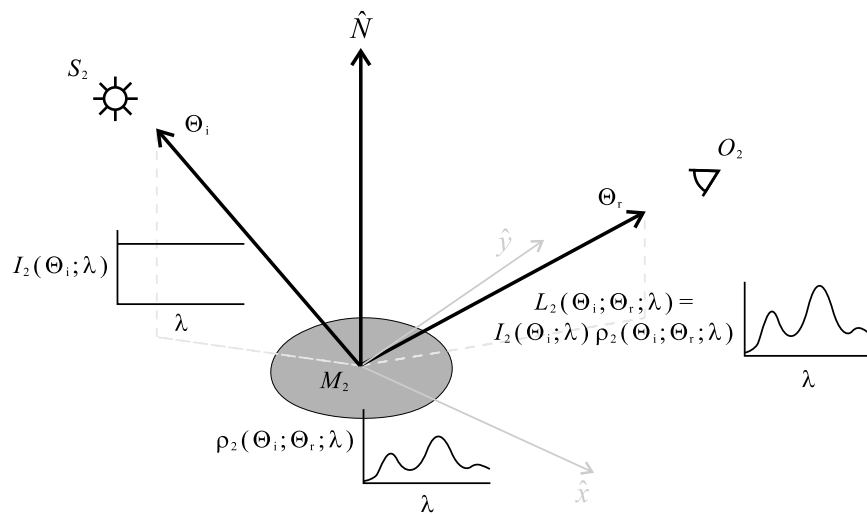


FIGURE 21. Observed radiance using simplified spectral method

(Figure 22). It was shown above that surface reflectance properties can be modified to produce the correct spectral distribution of radiance from a spectrally uniform light source. In the same way, Figure 23 diagrams how the material's reflectance can be represented with RGB values, specified so as to modify a source of uniform RGB in order to produce the same RGB values as Figure 22. The BRDFs assigned to material  $M_2$  are computed from the tristimulus values of material  $M_1$  by the following equations:

$$\rho_R(\Theta_i; \Theta_r) = \frac{R_1(\Theta_i; \Theta_r)}{\pi R_{max}} \quad (4.2)$$

$$\rho_G(\Theta_i; \Theta_r) = \frac{G_1(\Theta_i; \Theta_r)}{\pi G_{max}} \quad (4.3)$$

$$\rho_B(\Theta_i; \Theta_r) = \frac{B_1(\Theta_i; \Theta_r)}{\pi B_{max}} \quad (4.4)$$

where  $R_{max}$ ,  $G_{max}$ , and  $B_{max}$  are the maximum <sup>1</sup> values assigned to the RGB color scale. The denominator values scale the BRDFs so that direct reflectance of the reference light source off a perfect diffuser results in a computed BRDF of  $1/\pi$  for all three color channels. With this technique, a scene which utilizes only tristimulus values for source and material reflectance will result in the same final tristimulus values as one which incorporates the full spectral representation throughout.

This method has its limitations. In particular, significant interreflections between surfaces with high spectral variability should be avoided. This also applies to self reflection, so convex objects are preferable. Reflection off gray surfaces (equal energy at all wavelengths) will not produce any difference between the two representations. It is

---

<sup>1</sup>Colorimetry is typically defined for Lambertian surfaces. The maximum value is defined as the value obtained by direct reflection of the reference light source off a perfect diffuser. Clearly this maximum value can be exceeded in the context of a non-Lambertian surface, where the BRDF value can approach infinity.



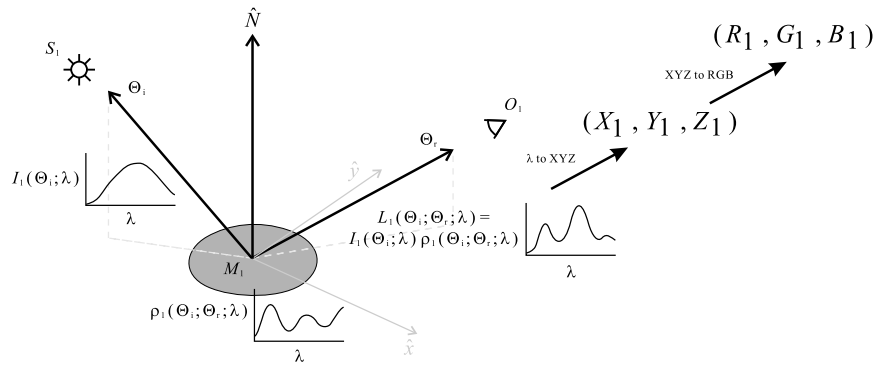


FIGURE 22. Observed tristimulus values using normal RGB method

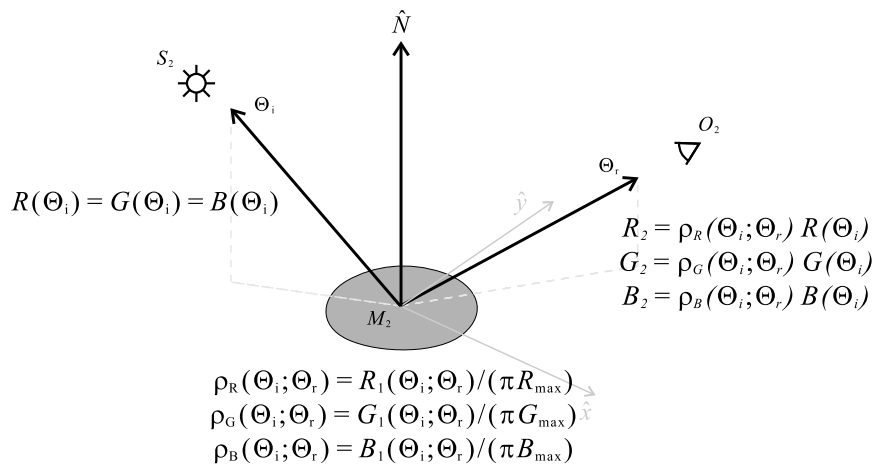


FIGURE 23. Observed tristimulus values using simplified RGB method

also important to realize that the spectrum of the source is bound at the point of its conversion to tristimulus values. In order to utilize a light source with a different spectral distribution, the tristimulus values must be recalculated or remeasured.

When applied to the determination of the BRDF of metallic or pearlescent paints, the rather daunting task of measuring the tristimulus values at all possible incident and reflected directions as required by (4.2) through (4.4) is greatly simplified by using Alman's method. As described above, Alman proposed the measurement of those surfaces at three critical aspecular angles (i.e., near-specular, face, and flop) with interpolation at other angles performed in CIELAB space. Although Alman's original work was related to measurement and interpolation within the plane of incidence, good results have been achieved by extending this to measurements out of plane, defining the aspecular angle to be

$$\theta_\alpha = \text{acos}((\Theta_i - 2\Theta_i \cdot \hat{n}) \cdot \Theta_r),$$

the angle between the reflected and specular directions. Thus the four spatial dimensions of the BRDFs presented in (4.2) through (4.4) can be reduced to one:

$$\rho_R(\Theta_i; \Theta_r) = \rho_R(\theta_\alpha) = \frac{R_1(\theta_\alpha)}{\pi R_{max}} \quad (4.5)$$

$$\rho_G(\Theta_i; \Theta_r) = \rho_G(\theta_\alpha) = \frac{G_1(\theta_\alpha)}{\pi G_{max}} \quad (4.6)$$

$$\rho_B(\Theta_i; \Theta_r) = \rho_B(\theta_\alpha) = \frac{B_1(\theta_\alpha)}{\pi B_{max}}. \quad (4.7)$$

This technique of BRDF determination was applied to six metallic paint samples for which tristimulus values were measured using the five common aspecular angles, 15, 25, 45, 75, and 110 degrees. Figures 24, 25, and 26 show the corresponding  $L^*$ ,  $a^*$ , and  $b^*$  values interpolated using a second degree polynomial of best fit as recommended

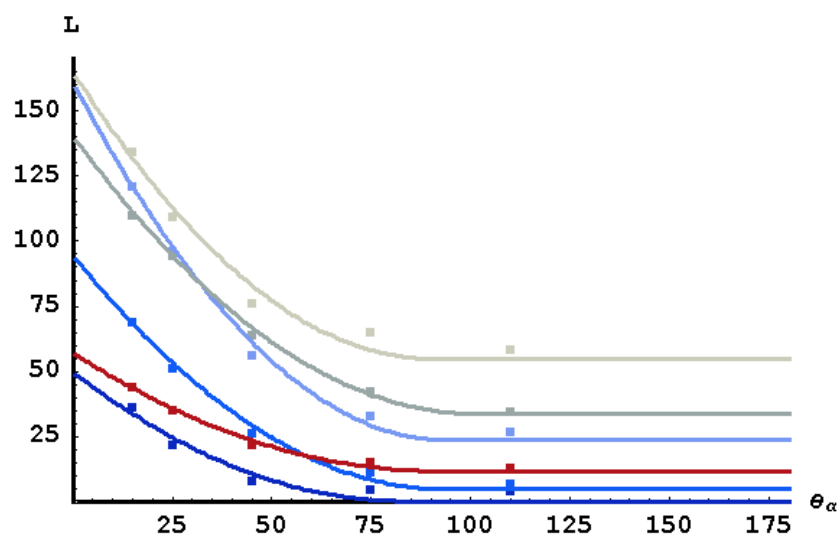


FIGURE 24.  $L^*$  values vs. aspecular angle for metallic paint samples

by Alman. The curves are clamped at the zero point of the first derivative to ensure monotonicity. Next, the interpolated  $L^*$ ,  $a^*$ , and  $b^*$  values are converted to RGB as is the source (which is CIE illuminant D65). Lastly these RGB values are used in (4.5), (4.6), and (4.7) to compute the BRDFs, shown in Figures 27, 28, and 29, of the metallic paint samples.

An image (Figure 30) of a scene consisting of three vases modeled with the computed metallic BRDFs was rendered in Radiance using the iBRDF extension (as described in Chapter II). The expected change in lightness is readily apparent on the surface of the vases, giving them a strong sense of metallic reflection. Another set of vases with three additional metallic paints is shown in Figure 31.

### First Surface Reflection - Gloss and Haze

Upon cursory examination, gloss is a rather simple surface appearance attribute; a surface is either glossy or matte. However the subtleties of gloss which are missed

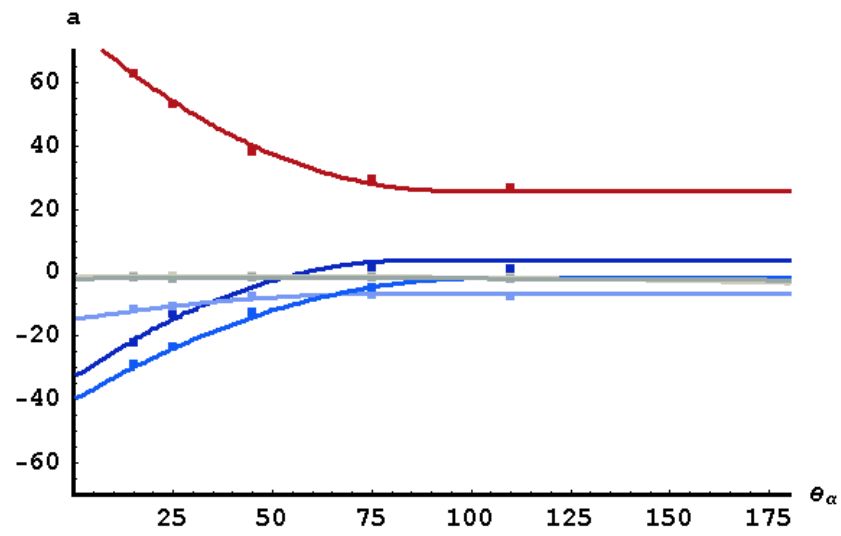


FIGURE 25.  $a^*$  values vs. aspecular angle for metallic paint samples

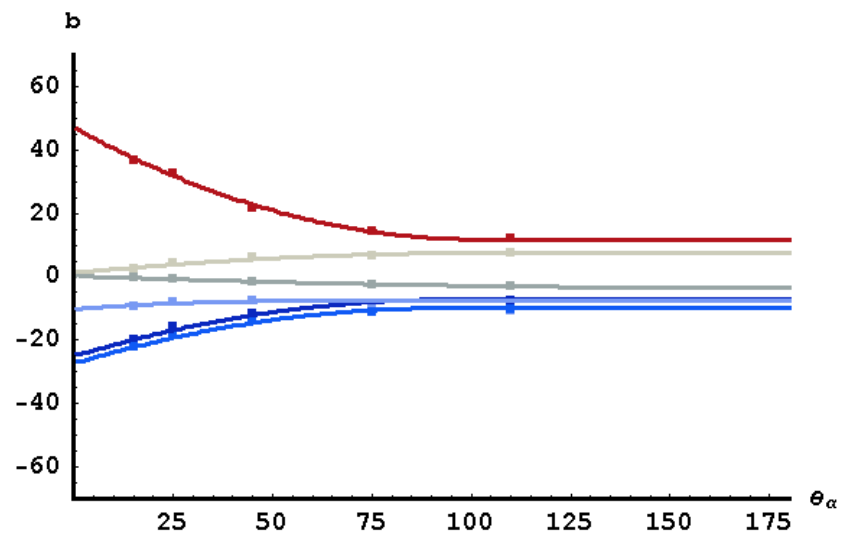
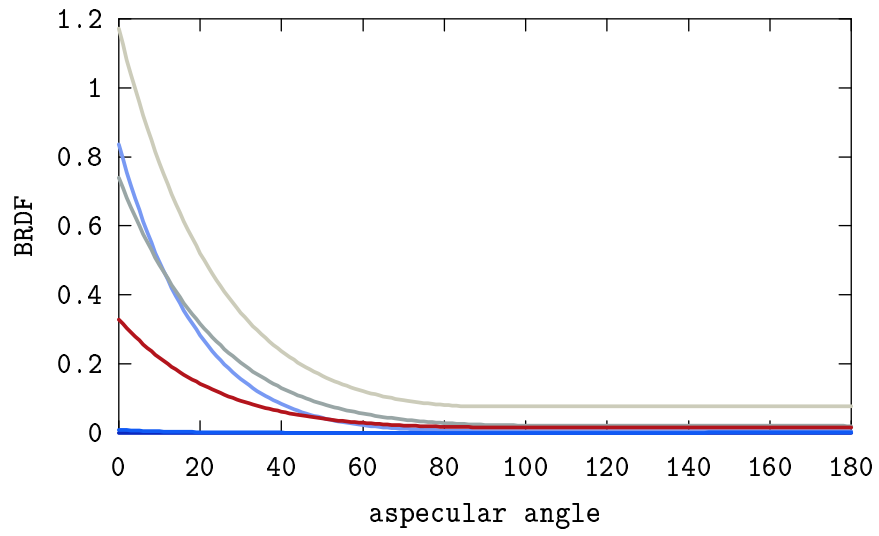
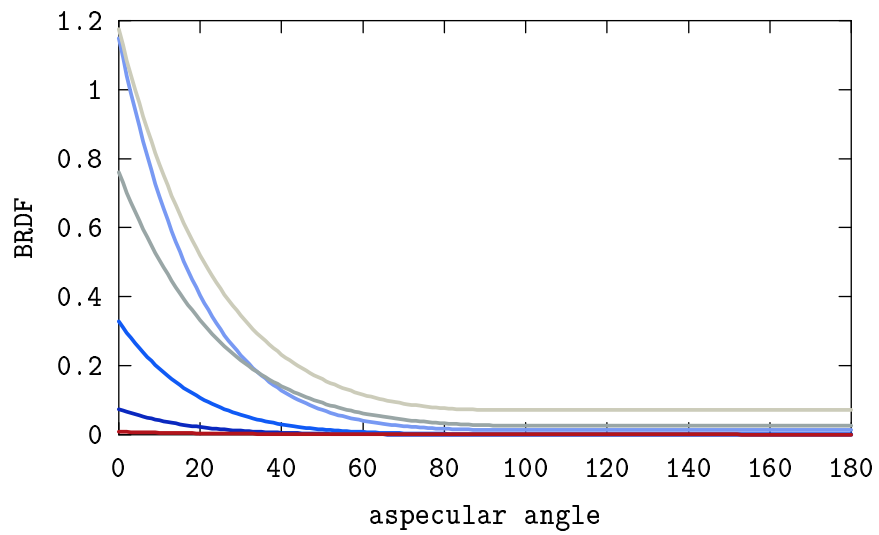


FIGURE 26.  $b^*$  values vs. aspecular angle for metallic paint samples

FIGURE 27.  $\rho_R(\theta_\alpha)$  vs.  $\theta_\alpha$  of metallic paint samplesFIGURE 28.  $\rho_G(\theta_\alpha)$  vs.  $\theta_\alpha$  of metallic paint samples

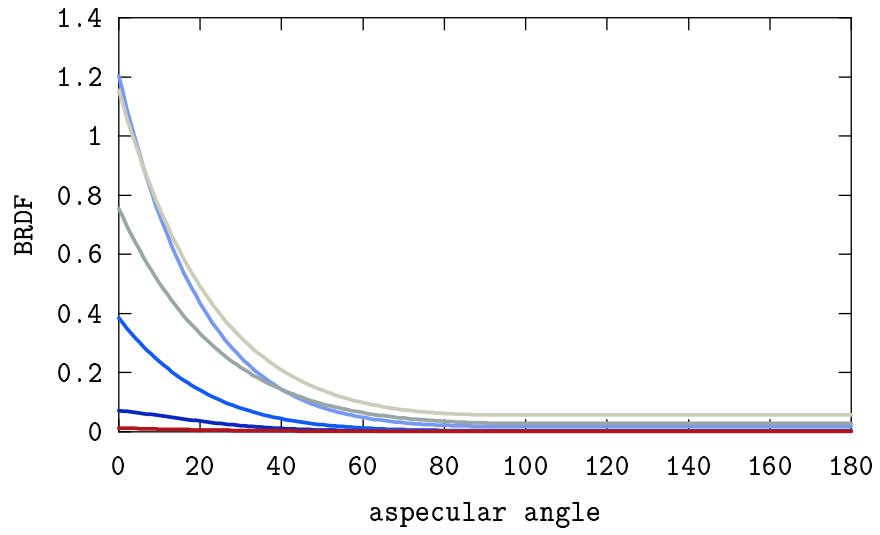


FIGURE 29.  $\rho_B(\theta_\alpha)$  vs.  $\theta_\alpha$  of metallic paint samples

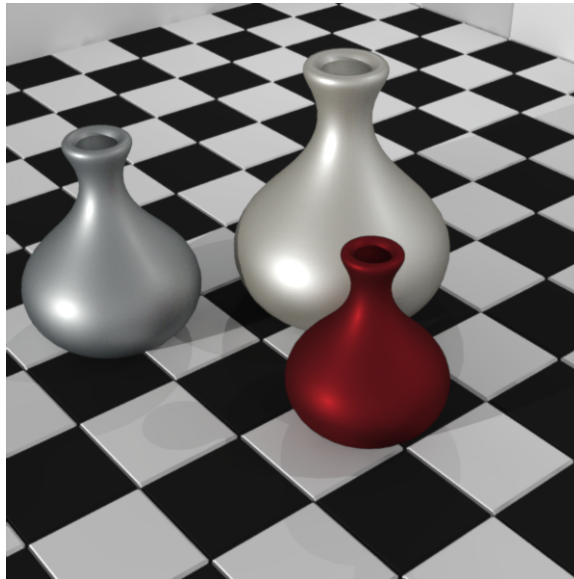


FIGURE 30. Three vases with metallic paint

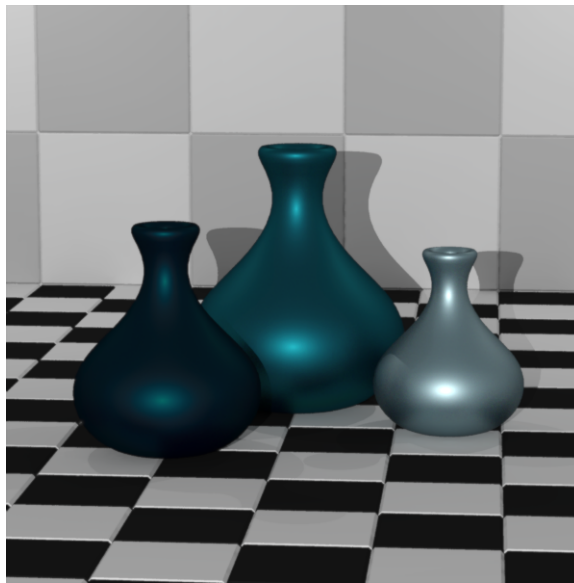


FIGURE 31. Three more vases with metallic paint

on this conscious examination are easily captured by the subconscious. These subtleties indirectly tell us whether a shirt is satin or nylon and inform us that it's time to clean the bathroom mirror. These are the same subtleties that have pushed industry to come up with ways to both quantify and to measure gloss.

#### Current Standards

Gloss is defined by the ASTM to be “the angular selectivity of reflectance, involving surface-reflected light, responsible for the degree to which reflected highlights or images of objects may be seen as superimposed on a surface” [5]. The seminal work on gloss measurement was performed by Hunter beginning in the 1930s. This work led him in 1937 to the differentiation of no less than six types of gloss: specular gloss, sheen, contrast gloss (or luster), absence-of-bloom gloss, distinctness of image gloss, and surface-uniformity gloss [32]. Categorizing gloss helped to quantify its subtleties

and led to the first standardized measurement of gloss, ASTM method D523-39, Test for Specular Gloss [34]. This standard method, which survives actively to this day, measures the light reflected in the specular direction off the sample surface, 60 degrees down from surface normal. A surface of high gloss will reflect most light in the specular direction while a surface with low gloss (e.g., a Lambertian surface) will reflect most of its light in directions other than specular. The numerical gloss value,  $G$ , assigned to a surface typically ranges from 100 (high gloss) to 0 (low gloss).

A primary goal in establishing standard gloss measurements is to create an instrumental measurement with a scale that mimicks the numerical appraisal of an appearance professional. Because of the wide range of gloss values it was found that the correlation between gloss values for the 60 degree specular gloss meter and equivalent human assigned values were valid for too small a range of glossiness. Better correlation for specular gloss was achieved by adding two more instruments, one which measured specular gloss at grazing angles (termed sheen by Hunter) and another which measured specular gloss at near normal angles. These two measurements now are also part of ASTM D523, which assigns the angles from normal to be 85 degrees and 20 degrees respectively. Results have confirmed that the 20, 60 and 85 degree specular gloss measurements offer numerical values which is roughly linearly correlated over a range of values to perceived gloss of high-gloss, medium-gloss, and low-gloss surfaces respectively [33]. Figure 32 shows a graphical comparison of measured to perceived gloss for different specular gloss standards.

Among other standards that are important to industry are haze and distinctness-of-image gloss measurements specified in ASTM E430 [6]. These measurements compare the light reflected directly in the specular direction to that reflected in the slightly off-



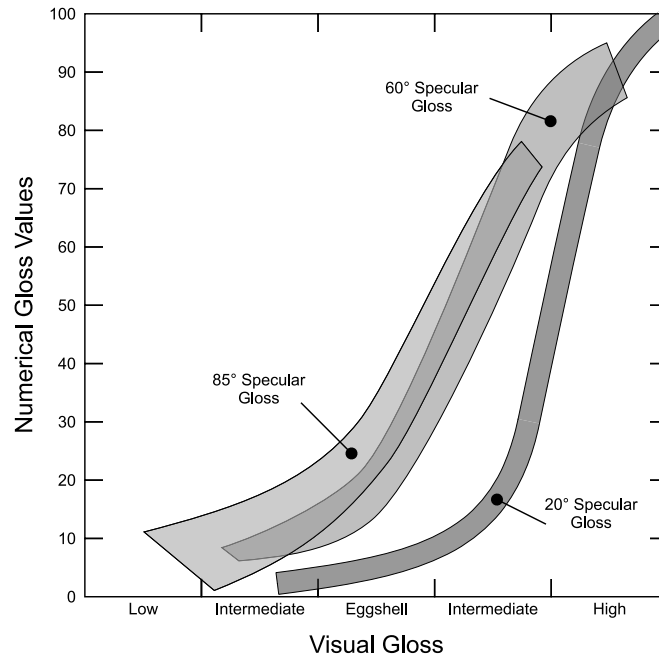


FIGURE 32. Numerical gloss values vs. visual gloss rating for ASTM specular gloss standards (after Hunter [33])

specular direction. For distinctness-of-image gloss, the angle of offset is essentially “as close as we can get” – centered a mere 0.3 degrees off of specular. This is to mimic the keen discrimination the human visual system has for detecting the sharpness of the reflection of an object in a highly reflective surface [33]. The quantity measured is  $G_{doi}$  which varies as with specular gloss; a larger value of  $G_{doi}$  corresponds to a more distinct image (i.e., a higher gloss value). The two haze measurements specified in ASTM E430 offer better correlation to the perceived haziness of surfaces with more directionally diverse surface scatter. The haze value is a measure of the similarity between the pure specular reflection (measured with 30 degree gloss) and off-specular reflection (measured either 2 or 5 degrees off specular). One more haze measurement is specified in ASTM D4039 [3], which utilizes the difference between the 20 and 60 degree specular gloss measurements. This haze measurement takes advantage of the difference in

TABLE 1. Standard gloss and haze measurement specifications (after Hunter [33]). Aperture fields are measured as (in plane of measurement) $\times$ (perpendicular to plane of measurement). Values are taken from from ASTM [4, 6].

Gloss	ASTM Standard	Specular Angle	Aspecular Angle	Aperture Field (in degrees)	
				Source	Receptor
Specular gloss	D523	20°	0°	0.75 $\times$ 2.5	1.8 $\times$ 3.6
Specular gloss	D523	60°	0°	0.75 $\times$ 2.5	4.4 $\times$ 11.7
Specular gloss (sheen)	D523	85°	0°	0.75 $\times$ 2.5	4.0 $\times$ 6.0
Specular gloss	E430	30°	0°	0.44 $\times$ 5.0	0.4 $\times$ 3.0
Distinctness-of-image	E430	30°	$\pm 0.3^\circ$	0.44 $\times$ 5.0	0.14 $\times$ 3.0
Haze	E430	30°	$\pm 2^\circ$	0.44 $\times$ 5.0	0.4 $\times$ 3.0 or 0.5 $\times$ 3.0
Haze	E430	30°	$\pm 5^\circ$	0.44 $\times$ 5.0	0.4 $\times$ 3.0 or 0.5 $\times$ 3.0

the sizes of detector apertures of the two gloss measurements to measure specular and off-specular reflection. The convention used for the measured value of haze,  $H$ , is an increasing numerical value associated with increasing haziness.

A more detailed list of the above standards specifications is listed in Figure 1. The ASTM provides a complete description of all these standards, updated annually [2]. An excellent overview of these appearance measurement standard is offered by Hunter [33]. In addition, Hunter includes a discussion of other appearance based standards relating to specific industries.

### Virtual Light Meter

The measure of gloss is a simplification of the BRDF down to a single appearance related quantity. Using a BRDF model as the representation of light reflection in com-

puter graphics affords subtle appearance detail but also presents difficulty in selecting the correct BRDF model parameters. What is necessary is a way to develop a correspondence between BRDF model parameters and standard appearance measurements. A virtual light meter was constructed for this purpose. In the same way that various gloss meters give control over surface reflection properties to the product engineer, a virtual light meter can give control over BRDF model parameters to the computer graphics appearance designer.

The virtual light meter is essentially a customized integration tool, using numerical quadrature of the specified BRDF model over an adaptively subdivided source and receptor aperture (Figure 33) to compute the final standard appearance value. In addition to being able to calculate the standards (specular gloss, distinctness-of-image, and haze) the virtual light meter can be customized for other measurements. The customizable parameters include the size and locations of the source and receptor apertures, the specular angle, the surface orientation, and the reflection model.

Gloss values are directly dependent upon the measured flux reflected off the surface and passing through the receptor aperture. The integration of this flux begins by subdividing the source aperture. For each sample point on the source, the receptor aperture is subdivided. Based on the initial results of the integration, the receptor aperture is adaptively subdivided until the discretely computed flux is within some specified tolerance. Figure 34 shows an example of the flux due to one subdivided source element passing through the receptor. After this flux is determined, the next source sample point is chosen and the process is repeated. The source aperture continues to be subdivided until a specified tolerance is achieved. More detail of the integration process is offered below.

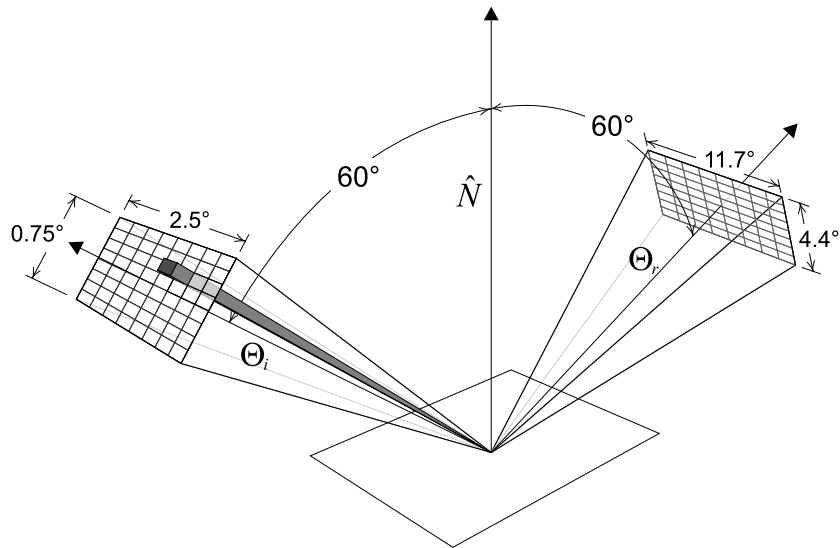


FIGURE 33. Subdivision of source and receptor apertures using 60 degree gloss specifications. The apertures are not to scale.

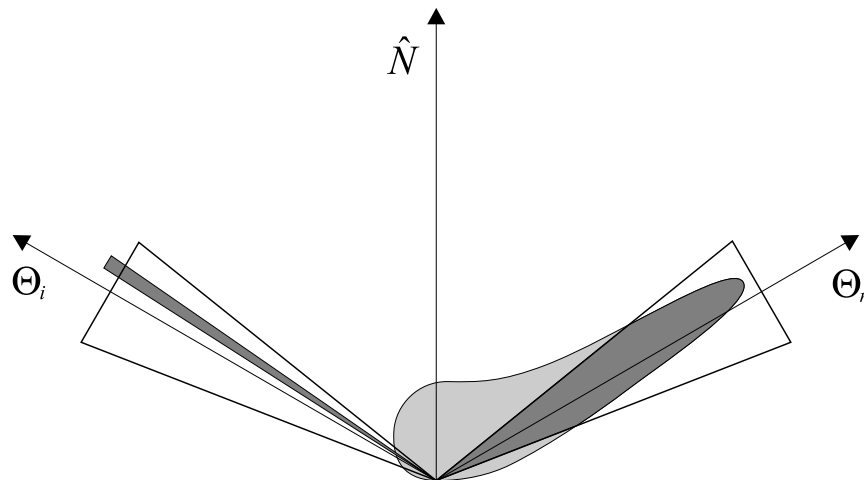


FIGURE 34. Flux passing through receptor aperture due to one source aperture subdivision. Aperture sizes are not to scale.

TABLE 2. 20 degree specular gloss values computed from the Ward model over a range of roughness values

$\sigma$	$G_{20}$	$\sigma$	$G_{20}$	$\sigma$	$G_{20}$
0.004	99.0	0.013	51.8	0.022	26.2
0.005	95.3	0.014	47.8	0.023	24.5
0.006	90.3	0.015	44.1	0.024	23.0
0.007	84.4	0.016	40.7	0.025	21.5
0.008	78.3	0.017	37.7	0.026	20.2
0.009	72.2	0.018	35.0	0.027	19.0
0.01	66.5	0.019	32.5	0.028	17.9
0.011	61.2	0.02	30.2	0.029	16.9
0.012	56.3	0.021	28.1	0.03	15.9

This virtual light meter allows the user to determine the specular gloss, distinctness-of-image, haze, etc. produced by a BRDF model with specified parameter values. To find the model parameters required to achieve a desired appearance value, the program can be run several times using different BRDF parameter values. Table 2 lists the computed 20 degree gloss values of the isotropic Ward model, (2.17), with varying roughness values. The same values are graphed using linear interpolation in Figure 35. The same linear interpolation can be used to determine the roughness parameter required to achieve a desired gloss value. For example, the roughness required to produce a 20 degree specular gloss value of 50, using linear interpolation of the data in Table 2, is  $\sigma = 0.01445$ .

### The Integration Method

To perform the integration over source and receiver apertures, the numerical cubature library tool Cubpack++ was used. Cubpack++ is an extensive C++, template based, class library for adaptive numerical integration of functions over two-dimensional areas [18, 19, 20, 21].

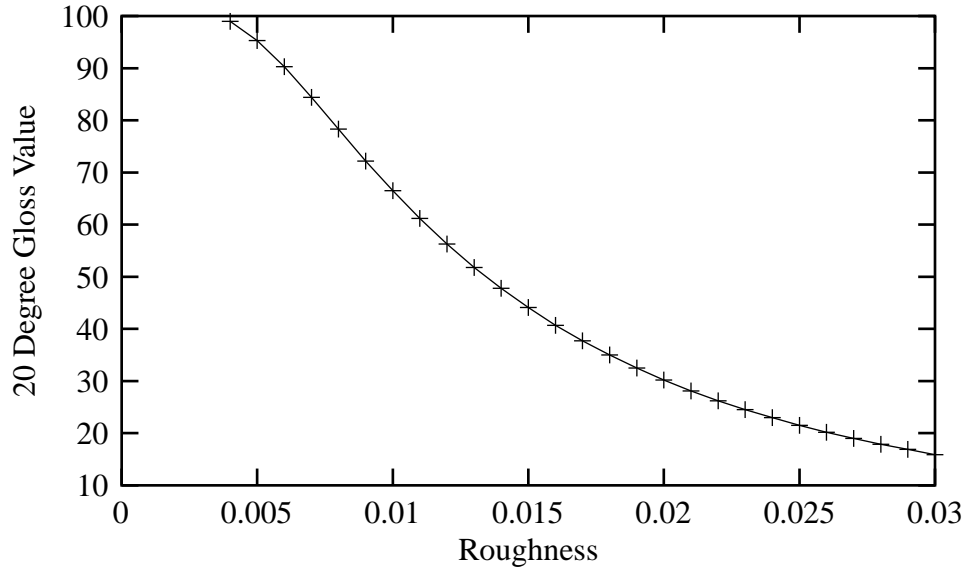


FIGURE 35. 20 degree specular gloss values vs. roughness from the Ward model

The rectangularly defined source and detector apertures are both subdivided adaptively by Cubpack++. Integration over the aperture which exists in world 3D space is achieved by coordinate transformation to local (i.e., aperture) 2D space. The rectangular ASTM definition of the aperture is particularly convenient for use in this cubature library since rectangles are primitive integration geometries. The surface irradiance due to each subdivided element of the source is modified by the sample BRDF and geometric conditions to find the flux at each detector patch. Rather than using the flux directly, we will discuss the integration process with respect to radiant exitance, the exitent flux density:

$$M \equiv \frac{d\Phi}{dA}.$$

The irradiance at surface element  $dA$  due to  $S_j$ , the  $j^{\text{th}}$  patch of the source aperture, is

$$dE_{S_j} = L_S \hat{\mathbf{s}}_j \cdot \hat{\mathbf{n}} d\omega_{S_j} \quad (4.8)$$

where  $L_S$  is the radiance of the source,  $\hat{\mathbf{s}}_j$  is the unit direction vector of  $S_j$ ,  $\hat{\mathbf{n}}$  is the unit normal vector to  $dA$ , and  $d\omega_{S_j}$  is the solid angle subtended by  $S_j$  at  $dA$ . The resulting surface radiance is the product of this irradiance and  $\rho(\hat{\mathbf{s}}_j; \hat{\mathbf{r}})$ , the BRDF of the surface:

$$dL(\hat{\mathbf{s}}_j; \hat{\mathbf{r}}) = \rho(\hat{\mathbf{s}}_j; \hat{\mathbf{r}}) dE_{S_j} \quad (4.9)$$

where  $\hat{\mathbf{r}}$  is the unit direction vector of the exitent radiance. The radiant exitance can then be found at  $D_k$ , the  $k^{th}$  patch of the detector aperture by choosing the exitent direction of radiance to be the direction of the detector patch.

$$d^2 M_{S_j, D_k} = dL(\hat{\mathbf{s}}_j; \hat{\mathbf{d}}_k) \hat{\mathbf{d}}_k \cdot \hat{\mathbf{n}} d\omega_{D_k} \quad (4.10)$$

or

$$d^2 M_{S_j, D_k} = \rho(\hat{\mathbf{s}}_j; \hat{\mathbf{d}}_k) L_S \hat{\mathbf{s}}_j \cdot \hat{\mathbf{n}} d\omega_{S_j} \hat{\mathbf{d}}_k \cdot \hat{\mathbf{n}} d\omega_{D_k} \quad (4.11)$$

where  $\hat{\mathbf{d}}_k$  is the unit direction vector of  $D_k$  and  $d\omega_{D_k}$  is the solid angle subtended by  $D_k$  at  $dA$ .

In order to simplify notation, it is common to write surface energy equations in terms of the projected solid angle rather than the solid angle. Doing so, equation 4.11 becomes

$$d^2 M_{S_j, D_k} = \rho(\hat{\mathbf{s}}_j; \hat{\mathbf{d}}_k) L_S d\Omega_{S_j} d\Omega_{D_k} \quad (4.12)$$

where  $d\Omega_{S_j}$  and  $d\Omega_{D_k}$  are the projected solid angles of the source and detector patches respectively.

The total radiant exitance passing through the detector is then the double integral of  $d^2 M_{S_j, D_k}$  over both apertures. We approximate this by using the double sum and

selecting an appropriately high subdivision for each aperture.

$$M_{S,D} = \sum_{k=1}^K \sum_{j=1}^J \rho(\hat{\mathbf{s}}_j; \hat{\mathbf{d}}_k) L_S d\Omega_{S_j} d\Omega_{D_k} \quad (4.13)$$

The source radiance,  $L_S$ , is constant so this can be brought out of the double sum:

$$M_{S,D} = L_S \sum_{k=1}^K \sum_{j=1}^J \rho(\hat{\mathbf{s}}_j; \hat{\mathbf{d}}_k) d\Omega_{S_j} d\Omega_{D_k}. \quad (4.14)$$

We now make the assumption that the radiant exitance is constant over the total illuminated surface area  $A$ . With this assumption, the total exitent flux passing through the detector aperture is:

$$\begin{aligned} \Phi_{S,D}(\rho) &= A M_{S,D} \\ &= A L_S \sum_{k=1}^K \sum_{j=1}^J \rho(\hat{\mathbf{s}}_j; \hat{\mathbf{d}}_k) d\Omega_{S_j} d\Omega_{D_k} \end{aligned} \quad (4.15)$$

The BRDF,  $\rho$ , is explicitly listed as parameter of  $\Phi$  to add clarity for when we later compare the exitent flux resulting from different surfaces.

### Deriving Gloss Values

We now give an example of how the flux computed from the previous sub-section can be used to find a numerical standard gloss value. The gloss value chosen for discussion is the specular gloss, but similar techniques are used to derive the other gloss values.



The specular gloss defined by ASTM D523 is

$$G = 100 \frac{\Phi_{S,D}(\rho_{sample})}{\Phi_{S,D}(\rho_{standard})} \quad (4.16)$$

The standard surface is smooth black glass with a refractive index of 1.567. The blackness limits the exitent flux to that which is produced from first surface reflection while the smoothness ensures that the reflection is all in the specular direction. The BRDF of the standard is thus a function of the Fresnel reflectivity and a delta function:

$$\rho_{standard}(\hat{\mathbf{s}}_j; \hat{\mathbf{d}}_k) = \frac{F(n, \hat{\mathbf{s}}_j) \delta(\text{mirror}(\hat{\mathbf{s}}_j) - \hat{\mathbf{d}}_k)}{d\Omega_{D_k}} \quad (4.17)$$

where  $F$  is the Fresnel reflectivity for unpolarized light,  $n$  is the refractive index of the standard, and  $\text{mirror}(\hat{\mathbf{s}}_j)$  is the unit mirror direction vector of  $\hat{\mathbf{s}}_j$ . The mirror direction vector can be computed with:

$$\text{mirror}(\hat{\mathbf{s}}_j) = 2(\hat{\mathbf{s}}_j \cdot \hat{\mathbf{n}}) \hat{\mathbf{n}} - \hat{\mathbf{s}}_j. \quad (4.18)$$

The delta function is:

$$\delta(\bar{v}) = \begin{cases} 1 & \text{if } |\bar{v}| < \epsilon, \\ 0 & \text{if } |\bar{v}| \geq \epsilon. \end{cases}$$

Using (4.15) gives the flux reflected from the standard:

$$\Phi_{S,D}(\rho_{standard}) = A L_S \sum_{k=1}^K \sum_{j=1}^J F(n, \hat{\mathbf{s}}_j) \delta(\text{mirror}(\hat{\mathbf{s}}_j) - \hat{\mathbf{d}}_k) d\Omega_{S_j} \quad (4.19)$$

This is computed off line and stored as a constant, for efficiency. If, however, a cus-

tomized light meter specification utilized variable parameters, the standard flux value could easily be computed at run time.

Lastly, the computed flux of the sample and the standard are applied to 4.16 to determine the specular gloss value:

$$G = 100 \frac{\sum_{k=1}^K \sum_{j=1}^J \rho(\hat{\mathbf{s}}_j; \hat{\mathbf{d}}_k) d\Omega_{S_j} d\Omega_{D_k}}{\sum_{k=1}^K \sum_{j=1}^J F(\mathbf{n}, \hat{\mathbf{s}}_j) \delta(\text{mirror}(\hat{\mathbf{s}}_j) - \hat{\mathbf{d}}_k) d\Omega_{S_j}}. \quad (4.20)$$

As is expected, the sample area and source radiance drop out of the equation of gloss; specular gloss becomes a function of BRDF, index of refraction and geometry.

### Utilizing Gloss and Haze

Using a virtual light meter avoids some of the pitfalls of real light meters. Unlike a real world surface, a virtual surface modeled with an analytical BRDF doesn't have imperfections or variations to be concerned about. Whereas a real surface may have curves or macroscopic height variations, its mathematical counterpart can be assured to be perfectly flat. Also, by having precise mathematical definitions with defined tolerances, the virtual light meter avoids real world manufacturing and thus avoids variances between light meters.

While the analytical nature of the virtual light meter circumvents several real world difficulties, the same computational scheme can become problematic when used in the evaluation of a physically based measurement such as gloss. Real world surfaces are dominated by Fresnel effects, but this is not necessarily so with BRDF models. Gloss and haze meters are designed to utilize these Fresnel effects in measurements. For analytical BRDF models not utilizing Fresnel reflectance, the ASTM gloss measurements of 20, 60 and 85 degrees will generally produce variance only because of the variance

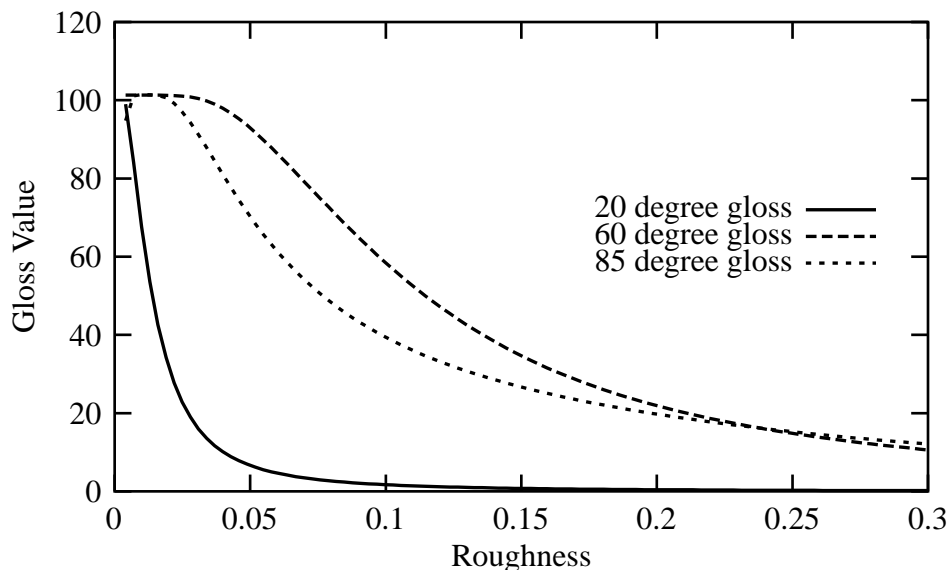


FIGURE 36. Gloss vs. roughness for Ward isotropic reflection model

of the receptor aperture size. Other potential conflicts exist regarding characteristics of physically implausible BRDFs such as lack of energy conservation and lack of reciprocity as discussed by Lewis [44] and Shirley [62]. There are still advantages to the simplification of these BRDFs down to a gloss or haze values, but the limitations must be kept in mind.

Several of the gloss attributes were computed for the Ward model as shown in Table 3. The corresponding data is plotted in Figure 36 for gloss and in Figure 37 for haze. These values use only the specular component of (2.17), setting  $\rho_d = 0$  and  $\rho_s = 1$ . The Ward model falls into the category of BRDFs not modified by the Fresnel reflectance. To compute gloss and haze values for the Ward model the flux of the standard in (4.19) was determined using a Fresnel term with a fixed value of one. This is similar to standardized methods of measuring gloss values of metallic samples which reflect almost all visible light [6].

TABLE 3. Gloss and haze values computed from the Ward model over a range of roughness values

$\sigma$	$G_{20}$	$G_{60}$	$G_{85}$	$H_2$	$H_5$
0.004	99.0	101.3	94.8	0.0	0.0
0.006	90.3	101.3	101.4	0.1	0.0
0.008	78.3	101.3	101.5	2.3	0.0
0.010	66.5	101.3	101.4	10.8	0.0
0.012	56.3	101.3	101.7	25.7	0.0
0.014	47.8	101.3	101.4	43.7	0.0
0.016	40.7	101.3	101.8	62.0	0.2
0.018	35.0	101.3	101.6	79.0	0.8
0.020	30.2	101.2	100.9	94.1	2.3
0.022	26.2	101.2	99.9	107.1	5.1
0.024	23.0	101.2	98.5	118.2	9.4
0.026	20.2	101.1	96.7	127.7	15.1
0.028	17.9	101.0	94.7	135.8	22.2
0.030	15.9	100.8	92.6	142.7	30.2
0.035	12.2	99.9	86.7	155.9	52.7
0.040	9.6	98.3	80.7	165.2	75.7
0.045	7.7	96.0	75.1	171.9	97.1
0.050	6.4	93.2	69.9	176.9	116.1
0.055	5.3	90.0	65.2	180.7	132.4
0.060	4.5	86.5	61.0	183.6	146.4
0.065	3.9	82.9	57.2	185.9	158.3
0.070	3.3	79.2	53.7	187.8	168.4
0.080	2.6	71.8	47.9	190.5	184.5
0.090	2.0	64.8	43.1	192.4	196.4
0.100	1.7	58.2	39.2	193.8	205.4
0.110	1.4	52.3	35.9	194.8	212.3
0.120	1.2	47.0	33.0	195.6	217.7
0.130	1.0	42.3	30.6	196.2	222.0
0.140	0.9	38.2	28.5	196.7	225.5
0.160	0.7	31.3	24.9	197.4	230.7
0.180	0.5	26.0	22.1	197.9	234.3
0.200	0.4	21.8	19.7	198.3	236.9
0.220	0.3	18.5	17.7	198.5	238.9
0.240	0.3	15.9	16.0	198.8	240.4
0.260	0.2	13.8	14.5	198.9	241.6
0.280	0.2	12.0	13.2	199.0	242.5
0.300	0.2	10.6	12.1	199.1	243.3

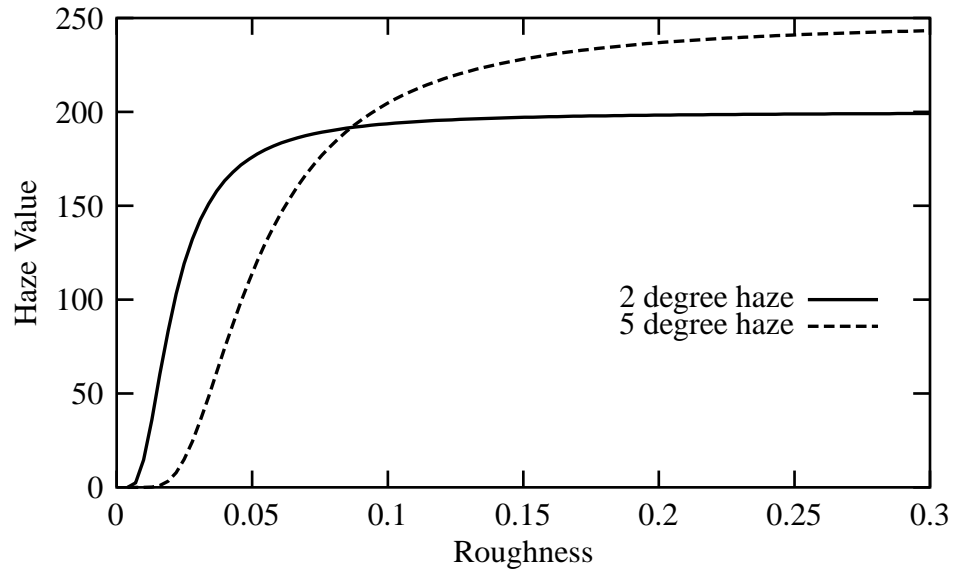


FIGURE 37. Haze vs. roughness for Ward isotropic reflection model

TABLE 4. Interpolated 20 degree specular gloss values for Ward isotropic reflection model

$G_{60}$	$\sigma$	$G_{60}$	$\sigma$	$G_{60}$	$\sigma$
10	0.0392	40	0.0162	70	0.0094
20	0.0262	50	0.0134	80	0.0077
30	0.0201	60	0.0112	90	0.0060

Using the interpolated 20 degree specular gloss values obtained from the Ward model, the roughness parameters required to obtain specular gloss in increments of 10 were determined and are displayed in Table 4. These roughness values were then used to render images of tiles using specular gloss values of 20, 40, 60, and 80 (Figure 38) and gloss values of 10, 30, 50, 70, and 90 (Figure 39). The goal of a linear appearance relationship between gloss value and appearance is achieved for both figures.

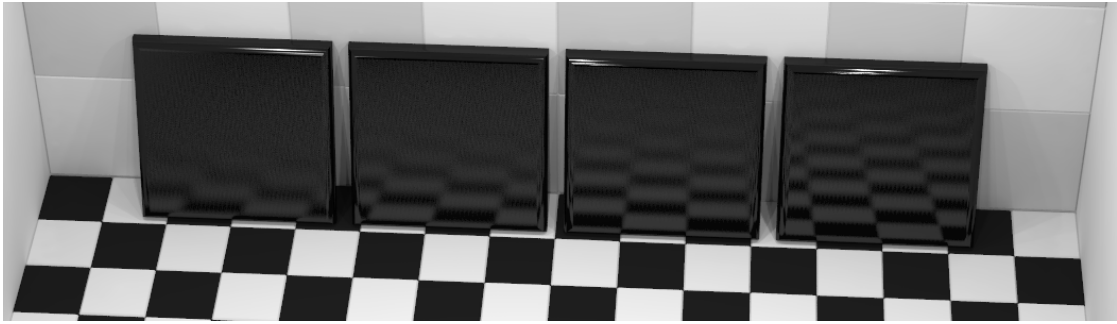


FIGURE 38. Tiles with measured 20 degree specular gloss values 20, 40, 60, and 80

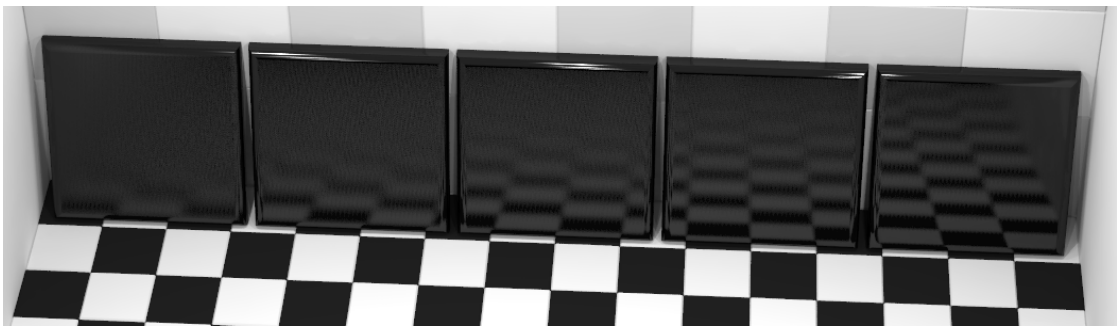


FIGURE 39. Tiles with measured 20 degree specular gloss values 10, 30, 50, 70, and 90

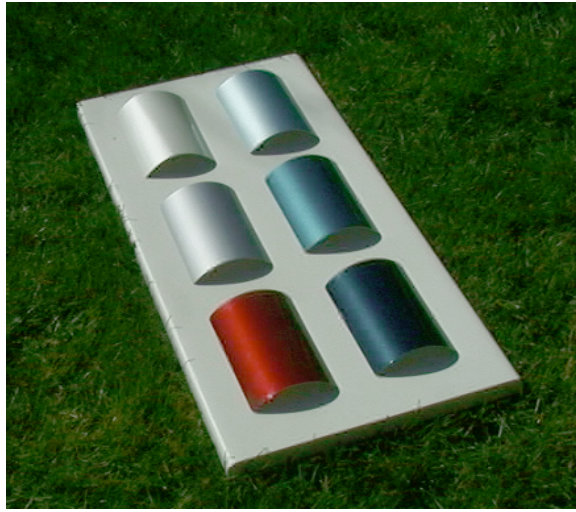


FIGURE 40. Photograph of clear coat finish on metallic paint

#### Combining First Surface and Flop

The two most important components of to the appearance of an object are its color and gloss. The above discussion provides a means of obtaining gloss and color values using tested and reliable measurements. These two attributes can then be combined to produce a more convincing synthetic image.

Consider the paint samples shown in Figure 40, each paint sample consists of metallic paint covered by a clear coat finish. Light incident on the surface is first scattered by the clear coat resulting in a perceived gloss of some measurable value. The remaining light enters the surface and some of this is reflected out based on the measurable flop values. Here we make the simplifying assumption that the total BRDF can be obtained by simple summation of the first surface and subsurface reflectances:

$$\rho = \rho_{fs} + \rho_{ss}.$$

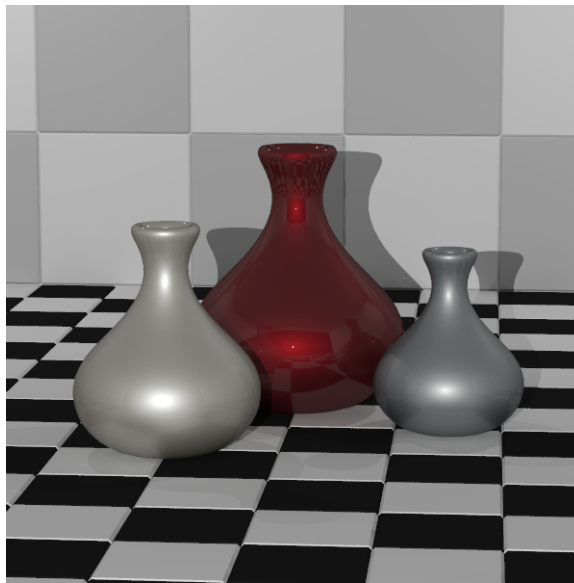


FIGURE 41. Three vases with metallic paint and a first surface of gloss 100

Figure 41 and Figure 42 shows vases modeled with the measured subsurface reflectance of metallic paint along with a first surface of perfectly reflecting ( $G = 100$ ) clearcoat finish. The images of Figure 43, Figure 44, and Figures 45 are rendered using a first surface reflection with a 20 degree specular gloss of 10 and 60. The first surface is achieved by using the Ward reflection model with surface roughness chosen to produce the particular gloss values.





FIGURE 42. Three more vases with metallic paint and a first surface of gloss 100

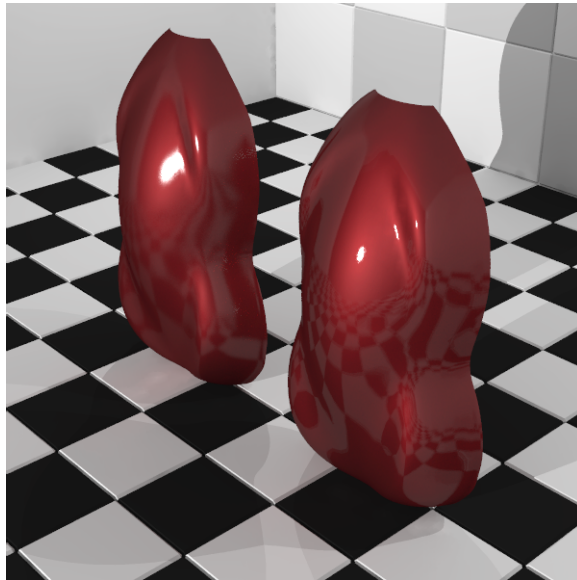


FIGURE 43. Two red automotive shells with 20 degree specular gloss of 10 and 60

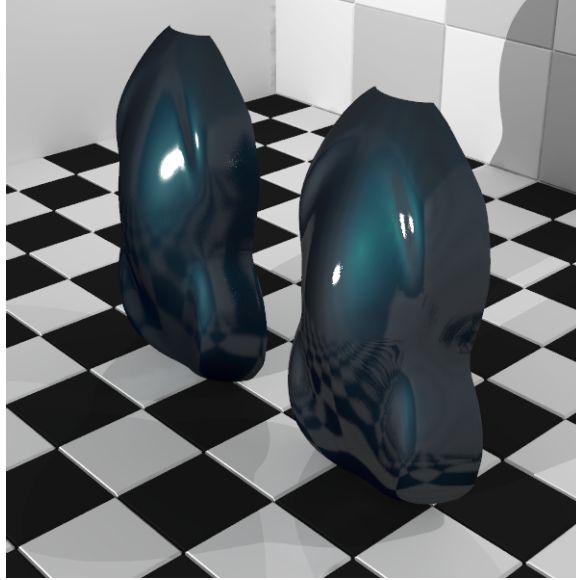


FIGURE 44. Two dark blue automotive shells with 20 degree specular gloss of 10 and 60

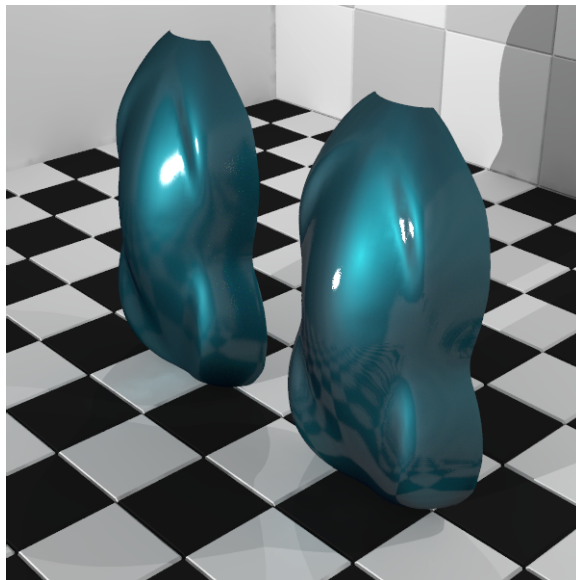


FIGURE 45. Two medium blue automotive shells with 20 degree specular gloss of 10 and 60

## CHAPTER V

### CONCLUSION

This thesis has offered several new realistic image synthesis tools to the computer graphics community. The ASTM standards and their associated measurement protocols can offer greater accuracy and control over the rendering process. Rendering efficiency can be enhanced with the use of a more general method of Monte Carlo importance sampling. Finally, a BRDF database, such as NEFDS, is a useful and practical synthetic imaging tool

The Monte Carlo integration technique presented in chapter II is an adaptive sampling method for arbitrary BRDFs. Since it only requires a table lookup, sampling is performed in constant time. Because of its speed and its flexibility, this technique, and Walker's alias method [70] on which it's based, should find application in other areas of computer graphics that are dependent upon Monte Carlo evaluation.

The Beard-Maxwell BRDF model discussed in chapter III provides a solid reflection model utilizing Fresnel reflectance, polarization, and directional diffuse scatter. Additionally, this BRDF model is empirically designed, providing a systematic way to utilize measured reflectance data. The corresponding BRDF database offers a wealth of new data for immediate use in realistic image synthesis. This database contains the BRDF model parameters for hundreds of measured surfaces.

The appearance of any surface can be characterized with well defined standards as was shown in chapter IV. Methods exist for modeling the reflection of light off metallic and pearlescent paints using only a few key measurements. These were used as the basis of a new BRDF model. Additional appearance standards such as gloss and haze offer simple yet powerful methods of capturing important BRDF data. This data can then be used to help specify the parameters of any BRDF model.

The measure of gloss and haze captures much of the microscopic height variation of surfaces. However, macroscopic variation due to dents, scratches and orange peel are not accounted for with these measurements. These other surface attributes are critical to the realistic modeling of an object and should also be considered. There are devices which are able to measure these effects (for example the BYK-Gardner wave-scan) which would be worthwhile to mimic in a similar virtual environment. Alternatively, if these height variation were represented with bump mapping [12] and the corresponding BRDF were generated [15], the current virtual light meter could be utilized.

The focus of this thesis is on methods to utilize real world data to specify a BRDF in order to generate more efficient or more accurate images. An alternative approach is to use the computer to design a BRDF (e.g., by simulation or parameter selection of an analytical model) which when applied to an object, produces the desired appearance. Once designed, the BRDF can then be used as the basis for a color scientist to create a real world surface with a matching BRDF (possibly making use of some of the appearance based standard measurements). Meyer has coined this computer-aided color appearance design (CACAD) [47], based on the similarity to the development and use of computer-aided design (CAD) in the engineering field.

Many of the ideas presented in this thesis are based heavily on previous work in other disciplines. Computer graphics is itself a relatively new discipline and can still greatly benefit from information hidden in other fields of study. This work should be an encouragement for others to continue to search other disciplines for yet undiscovered computer graphics tools.

## BIBLIOGRAPHY

- [1] David H. Alman. Directional color measurement of metallic flake finishes. In *Proceedings of the ISCC Williamsburg Conference on Appearance*, pages 53–56, 1987.
- [2] *Annual Book of ASTM Standards*, volume 06.01. American Society for Testing and Materials, Philadelphia, PA, 1999.
- [3] *ASTM D 4039-93, Standard Test Method for Reflection Haze of High-Gloss Surfaces*. Volume 06.01 of Annual Book of ASTM Standards [2], 1999.
- [4] *ASTM D 523-89, Standard Test Method for Specular Gloss*. Volume 06.01 of Annual Book of ASTM Standards [2], 1999.
- [5] *ASTM E 284-99a, Standard Terminology of Appearance*. Volume 06.01 of Annual Book of ASTM Standards [2], 1999.
- [6] *ASTM E 430-97, Standard Test Methods for measurement of Gloss of High-Gloss Surfaces by Goniophotometry*. Volume 06.01 of Annual Book of ASTM Standards [2], 1999.
- [7] Association Internationale de la Couleur (AIC). *Mondial Couleur 85, Proceeding of the 5th Congress of The International Color Association*, Paris, France, 1985.
- [8] Gorow Baba. Gonio-spectrophotometric analysis of pearl-mica paint. *Die Farbe*, 37:99–110, 1990.
- [9] Roy S. Berns. *Billmeyer and Saltzman's Principles of Color Technology*. John Wiley & Sons, Inc., New York, 3rd edition, 2000.
- [10] Robert Besold. Metallic effect - characterization, parameter and methods for instrumentally determination. *Die Farbe*, 37:79–85, 1990.
- [11] James F. Blinn. Models of light reflection for computer synthesized pictures. *Computer Graphics*, 11:192–198, 1977.
- [12] James F. Blinn. Simulation of wrinkled surfaces. *Computer Graphics (Proceedings of SIGGRAPH 78)*, 12(3):286–292, August 1978.
- [13] Tony Bridgeman. The reflection of metallic paints. In Association Internationale de la Couleur [7]. Article No. 5.

- [14] Gunter Buxbaum, editor. *Industrial Inorganic Pigments*. Weinheim, New York, 1993.
- [15] Brian Cabral, Nelson Max, and Rebecca Springmeyer. Bidirectional reflection functions from surface bump maps. *Computer Graphics (Proceedings of SIGGRAPH 87)*, 21(4):273–281, July 1987.
- [16] *Colorimetry*. Commission Internationale de L'eclairage, 2nd edition, 1986. Publication 15.2.
- [17] Robert L. Cook and Kenneth E. Torrance. A reflectance model for computer graphics. *ACM Transactions on Graphics*, 1:7–24, 1982.
- [18] Ronald Cools, Dirk Laurie, and Luc Pluym. Cubpack++. software: Numerical cubature class library.  
<ftp://ftp.cs.kuleuven.ac.be/pub/NumAnal-ApplMath/Cubpack/all.tar.gz>, Accessed November 10, 2000.
- [19] Ronald Cools, Dirk Laurie, and Luc Pluym. Cubpack++.  
<http://www.cs.kuleuven.ac.be/nines/research/cubpack/>, Accessed November 10, 2000.
- [20] Ronald Cools, Dirk Laurie, and Luc Pluym. Algorithm 764: Cubpack++ - a C++ package for automatic two-dimensional cubature. *ACM Transactions on Mathematical Software*, 23:1–15, 1997.
- [21] Ronald Cools, Dirk Laurie, and Luc Pluym. A user manual for Cubpack++. Technical Report TW 255, Katholieke Universiteit Leuven, Department of Computer Science, Leuven, Belgium, 1997. Version 1.1.
- [22] Ken Ellis. Reflectance phenomenology and modeling tutorial.  
<http://www.erim-int.com/on-line-docs/GUIDE/guide.frm.html>, Accessed September 10, 2000.
- [23] William Feller. *An Introduction to Probability Theory and Its Applications*, volume 1, chapter 10, pages 228–247. John Wiley & Sons, Inc., New York, 3rd edition, 1968.
- [24] George S. Fishman and L. Stephen Yarbber. Generating a sample from a  $k$ -cell table with changing probabilities in  $O(\log_2 k)$  time. *ACM Transactions on Mathematical Software*, 19(2):257–261, 1993.
- [25] Klaus-Dieter Franz. High luster mica pigments for automotive coatings. In Association Internationale de la Colour [7]. Article 70.

- [26] James E. Gentle. *Random Number Generation and Monte Carlo Methods*. Springer-Verlag New York, Inc., New York, 1998.
- [27] Cindy M. Goral, Kenneth E. Torrance, Donald P. Greenberg, and Bennett Battaile. Modelling the interaction of light between diffuse surfaces. *Computer Graphics (Proceedings of SIGGRAPH 84)*, 18(3):213–222, July 1984.
- [28] Donald P. Greenberg, Kenneth E. Torrance, Peter Shirley, James Arvo, James A. Ferwerda, Sumanta Pattanaik, Eric P. F. Lafortune, Bruce Walter, Sing-Choong Foo, and Ben Trumbore. A framework for realistic image synthesis. In *Proceedings of SIGGRAPH 97*, pages 477–494. Addison Wesley, August 1997.
- [29] Xiao D. He, Kenneth E. Torrance, François X. Sillion, and Donald P. Greenberg. A comprehensive physical model for light reflection. *Computer Graphics (Proceedings of SIGGRAPH 91)*, 25(4):175–186, July 1991.
- [30] Eugene Hecht. *Optics*. Addison Wesley Longman, Inc., 3rd edition, 1998.
- [31] Franz Hofmeister. Colourimetric evaluation of pearlescent pigments. In Association Internationale de la Colour [7]. Article 74.
- [32] Richard S. Hunter. Methods of determining gloss. *Journal of Research, NBS*, 17:77, 281, 1937. NBS Research Paper, RP 958.
- [33] Richard S. Hunter and Richard W. Harold. *The Measurement of Appearance*. John Wiley and Sons, Inc., New York, second edition, 1987.
- [34] Richard S. Hunter and Dean B. Judd. Development of a method of classifying paints according to gloss. *ASTM Bulletin*, (97):11, March 1939.
- [35] James T. Kajiya. The rendering equation. In *Computer Graphics, Annual Conference Series*, pages 143–150. ACM SIGGRAPH, 1986.
- [36] Donald E. Knuth. *Seminumerical Algorithms*, volume 2 of *The Art of Computer Programming*. Addison-Wesley Longman, Reading, Massachusetts, second edition, 1998.
- [37] R. A. Kronmal and A. V. Peterson. The alias and alias-rejection-mixture methods for generating random variables from probability distributions. In *Proceedings of the 1979 Winter Simulation Conference*, pages 269–280. Institute of Electrical and Electronics Engineers, 1979.
- [38] R. A. Kronmal and A. V. Peterson. On the alias method for generating random variables from a discrete distribution. *The American Statistician*, 33:214–218, 1979.



- [39] R. A. Kronmal and A. V. Peterson. A variant of the acceptance-rejection method for computer generation of random variables. *Journal of the American Statistical Association*, 76:446–451, 1981.
- [40] Eric P. F. Lafortune, Sing-Choong Foo, Kenneth E. Torrance, and Donald P. Greenberg. Non-linear approximation of reflectance functions. In *Proceedings of SIGGRAPH 97*, pages 117–126. Addison Wesley, August 1997.
- [41] J. H. Lambert. *Photometria sive de mensura et grabibus luminis, colorum et umbrae*. Eberhard Klett, Augsburg, Germany, 1760.
- [42] Greg Ward Larson and Rob Shakespeare. *Rendering with Radiance. The Art and Science of Lighting Visualization*. Morgan Kaufmann Publishers, Inc., San Francisco, 1998.
- [43] Gregory J. Ward Larson. Measuring and modeling anisotropic reflection. *Computer Graphics (Proceedings of SIGGRAPH 92)*, 26(2):265–272, July 1992.
- [44] Robert Lewis. Making shaders more physically plausible. *Fourth Eurographics Workshop on Rendering*, pages 47–62, June 1993.
- [45] J. R. Maxwell, J. Beard, S. Weiner, and D. Ladd. Bidirectional reflectance model validation and utilization. Technical Report AFAL–TR–73–303, Environmental Research Institute of Michigan (ERIM), October 1973.
- [46] C. S. McCamy. Observation and measurement of appearance of metallic materials. part I. macro appearance. *Color Research and Application*, 21(4), 1996.
- [47] Gary W. Meyer. Computer aided color appearance design. *Proceedings of the First International Conference on Color in Graphics and Image Processing*, 2000.
- [48] *NEF Specifications*, July 1996. ORD 258-96.
- [49] *NEF User Guide*, 9.1 edition. <http://ciks.cbt.nist.gov/nef/nefhome.html>, Accessed September 1, 2000.
- [50] F. E. Nicodemus, J. C. Richmond, J. J. Hsia, I. W. Ginsberg, and T. Limperis. Geometric considerations and nomenclature for reflectance. Technical Report MN-160, U.S. Department of Commerce, National Bureau of Standards, October 1977.
- [51] ASTM Committee E-12 on Appearance of Materials. *ASTM standards on color and appearance measurement*. American Society for Testing and Materials, Philadelphia, PA, sixth edition, 1996.

- [52] A. V. Peterson and R. A. Kronmal. On mixture methods for the computer generation of random variables. *The American Statistician*, 36:184–191, 1982.
- [53] Bui-T. Phong. Illumination for computer generated pictures. *Communications of the ACM*, 18(6):311–317, June 1975.
- [54] Radiance home page. <http://radsite.lbl.gov/radiance/index.html>. Accessed September 1, 2000.
- [55] Allan B. J. Rodrigues. Color vision in instrumental color matching. *16th International Conference in Organic Coatings*, 1990.
- [56] Allan B. J. Rodrigues. Measurement of metallic and pearlescent colors. *Die Farbe*, 37:65–78, 1990.
- [57] Allan B. J. Rodrigues. Color and appearance measurement of metallic and pearlescent finishes. *ASTM Standardization News*, 23(10):68–72, 1995.
- [58] Allan B. J. Rodrigues and Larry E. Steenhoek. Astm e-12.12: Measurement of metallic and pearlescent colors. *Die Farbe*, 42(4/6):151–158, 1996.
- [59] Gerhard Rösler. Multigeometry color measurements of effect surfaces. *Die Farbe*, 37:111–121, 1990.
- [60] Reuven Y. Rubinstein. *Simulation and the Monte Carlo method*. John Wiley & Sons, Inc., New York, 1981.
- [61] H. J. A. Saris, R.J.B. Gottenbos, and H. van Houwelingen. Correlation between visual and instrumental colour differences of metallic paint films. *Color Research and Application*, 15(4), 1990.
- [62] Peter Shirley, Helen Hu, Brian Smits, and Eric P. Lafortune. A practitioners' assessment of light reflection models. *Pacific Graphics '97*, October 1997.
- [63] Nicholas M. Short, Sr., Jim Rosalanka, Paul D. Lowman, Jr., Mitchell K. Hobish, William E. Stoney, Jeff Love, Jon W. Robinson, Matt Bechdol, and Jeff Weissel. The remote sensing tutorial. <http://rst.gsfc.nasa.gov/index.html>, Accessed September 14, 2000.
- [64] William C. Snyder, Zhengming Wan, and Xiaowen Li. Thermodynamic constraints on reflectance reciprocity and kirchoff's law. *Applied Optics*, 37(16):3464–3470, 1998.
- [65] Kenneth E. Torrance and E. M. Sparrow. Theory for off-specular reflection from roughened surfaces. *Journal of the Optical Society of America*, 57, September 1967.

- [66] Eric Veach. *Robust Monte Carlo Methods for Light Transport Simulation*. PhD thesis, Stanford University, 1997.
- [67] William H. Venable. A model for interpreting three-angle measurements of flake finishes. In *Proceedings of the ISCC Williamsburg Conference on Appearance*, pages 57–60, 1987.
- [68] Michael D. Vose. A linear algorithm for generating random numbers with a given distribution. *IEEE Transactions on Software Engineering*, 17:972–975, 1991.
- [69] A. J. Walker. Fast generation of uniformly distributed pseudorandom numbers with floating point representation. *Electronics Letters*, 10(41):553–554, 1974.
- [70] A. J. Walker. New fast method for generating discrete random numbers with arbitrary frequency distribution. *Electronics Letters*, 10(8):127–128, 1974.
- [71] A. J. Walker. An efficient method for generating discrete random variables with general distributions. *ACM Transactions on Mathematical Software*, 3:253–256, 1977.
- [72] Peter Andrew Walker. A visualization system for bidirectional reflectance distribution functions. Master’s thesis, University of Oregon, 1999.
- [73] Gregory J. Ward. Adaptive shadow testing for ray tracing. In P. Brunet and F. W. Jansen, editors, *Proceedings of the Second Annual Eurographics Workshop on Rendering*, Barcelona, 1991. Springer-Verlag.
- [74] Gregory J. Ward. The radiance lighting simulation and rendering system. In *Computer Graphics, Annual Conference Series*, pages 459–472. ACM SIGGRAPH, 1994.
- [75] Gregory J. Ward and Paul S. Heckbert. Irradiance gradients. In *Proceedings of the Third Annual Eurographics Workshop on Rendering*, Bristol, U.K., 1992. Springer-Verlag.
- [76] Gregory J. Ward, Francis M. Rubinstein, and Robert D. Clear. A ray tracing solution for diffuse interreflection. *Computer Graphics (Proceedings of SIGGRAPH 88)*, 22(4):85–92, August 1988.
- [77] Turner Whitted. An improved illumination model for shaded display. *Communications of the ACM*, 23(6):343–349, June 1980.

